

Graphical Abstract

A Hybrid Immersed-Boundary/Front-Tracking Method For Interface-Resolved Simulation of Droplet Evaporation

Faraz Salimnezhad, Hasret Turkeri, Iskender Gokalp, Metin Muradoglu

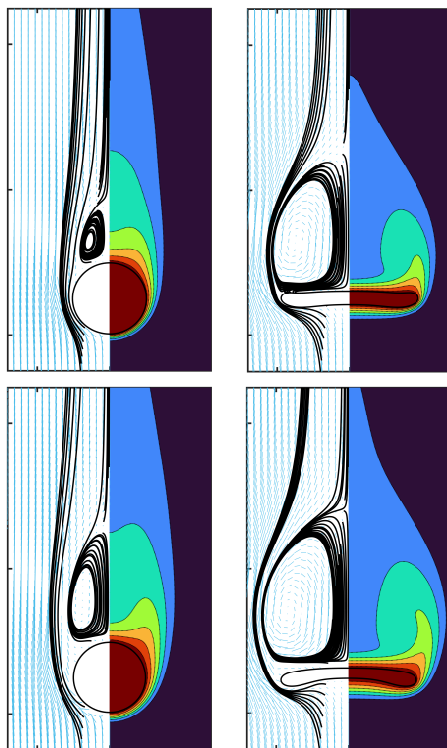


Figure 1: Effect of Stefan flow on the vapor mass fraction and flow fields around evaporating droplets including both nearly spherical and deforming cases.

Highlights

A Hybrid Immersed-Boundary/Front-Tracking Method For Interface-Resolved Simulation of Droplet Evaporation

Faraz Salimnezhad, Hasret Turkeri, Iskender Gokalp, Metin Muradoglu

- A hybrid IB/FT method is developed for simulating evaporation in multiphase flows.
- An image-point and ghost-cell method is used to enforce mass boundary conditions on droplets.
- The method is validated against benchmark test cases, demonstrating second-order spatial accuracy.
- The method is extended to simulate mass transfer from solid spheres in convective flows.
- The numerical results are compared with the existing evaporation models.

A Hybrid Immersed-Boundary/Front-Tracking Method For Interface-Resolved Simulation of Droplet Evaporation

Faraz Salimnezhad^a, Hasret Turkeri^b, Iskender Gokalp^c, Metin Muradoglu^a

^a*Koc University, Rumelifeneri Yolu, Sariyer, Istanbul, 34450, Turkey*

^b*Tusas Engine Industries (TEI), Tepebasi, Eskisehir, 26210, Turkey*

^c*Tubitak Marmara Research Center, Gebze, Kocaeli, 41470, Turkey*

Abstract

A hybrid sharp-interface immersed-boundary/front-tracking (IB/FT) method is developed for interface-resolved simulation of evaporating droplets in incompressible multiphase flows. A one-field formulation is used to solve the flow, species mass fraction and energy equations in the entire computational domain with appropriate jump conditions at the interface. An image point and ghost cell methodology is coupled with a front-tracking method to achieve an overall second order spatial accuracy for the mass fraction boundary condition on the droplet surface. The immersed-boundary method is also extended to simulate mass transfer from a solid sphere in a convective environment. The numerical method is first validated for the standard benchmark cases and the results are found to be in good agreement with analytical solutions. The method is shown to be overall second order accurate in space. Employing a moving reference frame methodology, the method is then applied to simulate evaporation of a deformable droplet in a convective environment and the results are compared with the existing evaporation models widely used in spray combustion simulations.

Keywords: Multiphase flows, droplet evaporation, phase change, direct numerical simulation, front-tracking method, sharp-interface immersed boundary method, evaporation models.

1. Introduction

Droplet evaporation is of fundamental importance in a wide range of natural phenomena and industrial applications [1, 2, 3, 4]. In particular, performance of spray combustion used in energy conversion devices such as internal combustion engines, gas turbines, liquid-fueled rocket engines and liquid-fueled industrial burners critically depends on liquid fuel atomization and droplet evaporation process in a convective environment [5, 3, 4]. Therefore, it is highly desirable to understand fuel droplet evaporation in a flowing ambient fluid for improving efficiency and power output of such devices. Droplet evaporation also plays a singularly vital role in the eventual fate of virus-laden droplets that are formed in the respiratory track [6, 2, 7].

Drop dynamics is highly complicated mainly due to the existence of the phase boundary (interface) that continuously deforms and may undergo topological changes in a complex flow field. Evaporation adds a further complexity making simulation of an evaporating droplet a challenging task especially in a convection dominated flow where thin mass boundary layer in the leading edge and a large flow separation behind the droplet need to be fully resolved [5, 3, 4].

Interface-resolved simulations of multiphase systems can give indispensable insight into underlying flow physics and help enhance understanding of evaporation process in applications ranging from heat exchangers and combustion engines to environmental processes such as cloud formation [8]. Several high-fidelity interface-resolved direct numerical simulation methods have been developed to tackle these challenges. The methods can be broadly categorized as the interface-capturing and the interface-tracking approaches [9]. In the interface-capturing methods, such as level-set (LS) and volume-of-fluid (VOF), the interface is represented implicitly by a color function. Interface-capturing methods have been widely used for interface-resolved simulations of interfacial flows mainly due to their implicit representation of interfaces in a fully Eulerian framework, which makes handling of topology change relatively easy and parallelization highly scalable, and good conservation properties especially in the presence of large jumps in material properties across phase boundaries. However, they suffer from the lack of precise information about location of interface which makes accurate computation of mass and energy exchange at the interface very difficult. Son and Dhir [10] pioneered the application of the level-set method to a phase change problem and studied film boiling in a two-dimensional setting. The level-set

method has become a popular choice in phase change simulations due to relatively easy treatment of interfacial jump conditions via coupling with the ghost fluid method [11, 12, 13, 14, 15, 16]. An important drawback of the level-set method has been reported as its poor conservation properties caused by the non-conservative nature of the level-set function [16]. On the other hand, the volume-of-fluid method, another popular interface-capturing technique, is appealing particularly due to its potential to achieve exact mass conservation regardless of grid resolution. However, in this approach, advection of the VOF color function has proved to be a challenging task limiting its widespread use in practical applications. Nevertheless, the VOF method has been successfully used to simulate various phase change problems [17, 18, 19, 20, 21, 22, 23, 24] since the pioneering work by Welch and Wilson [25] who developed the first VOF to investigate boiling flows in two-dimensional setup.

The front-tracking method used here has a distinct advantage of keeping interface sharp without any significant numerical diffusion and facilitating accurate evaluation of the flow and transport properties at the interface, thanks to the explicit representation of interface using a separate Lagrangian grid [26, 9]. The method has been successfully used to simulate a vast range of laminar and turbulent multiphase flows involving various multi-physics effects including phase change [27], soluble surfactant [28, 29], electric field [30], and complex fluid rheology [31]. Regarding the applications to the phase change problems, Juric and Tryggvason [27] developed a front-tracking method to simulate film boiling using an iterative method to satisfy the temperature boundary condition at the interface. Esmaeeli and Tryggvason [32, 33, 34] used essentially the same method but set the saturation temperature as a boundary condition on the interface to eliminate the need for an iterative procedure. Koynov et al. [35] employed a front-tracking method to study the buoyancy-driven motion of deformable bubbles accounting for one-way mass transfer from the bubble to the ambient fluid and chemical reactions in a wide range of operating conditions but they neglected the volume change due to mass transfer. Aboulhasanzadeh et al. [36] devised a multiscale method within the front-tracking framework for simulation of mass transfer from buoyant bubbles using a boundary layer approximation in the vicinity of the bubble to address the need for high grid resolution at high Schmidt numbers. Irfan and Muradoglu [37] developed a front-tracking method for interface-resolved simulation of evaporation process in a two dimensional setup using both the species-driven and the temperature-driven

evaporation models. In the follow up study, they also included chemical reactions to simulate a fuel droplet evaporation and combustion in an axisymmetric setup [38]. Khorram and Mortazavi [39] used a similar algorithm to simulate film boiling and bubble growth in a three dimensional setup but they also accounted for bubble breakup and coalescence using a novel topology change algorithm. Recently, Najafian and Mortazavi [40] improved this method to simulate droplet evaporation at high density ratio by advancing the front in two steps and solving the associated pressure Poisson equation twice to impose the mass conservation constraint.

In all the previous front-tracking methods, the species boundary condition at the interface is treated indirectly by conservatively distributing the evaporative mass flux as a source term outside the droplet near the interface using a one-sided distribution algorithm [37, 38, 40], which reduces the spatial accuracy significantly and results in a first order accuracy locally in general and globally in the strongly evaporating regimes [37]. As a result, an extreme grid resolution is usually required to reduce the spatial error below an acceptable level in strongly evaporating and convection dominating regimes, which is typically the case in combustion applications. This deficiency constitutes the main motivation in the present study. To address this issue, we develop a hybrid sharp-interface immersed-boundary/front-tracking (IB/FT) method that maintains an overall second order spatial accuracy and keeps the interface sharp. The main novelty is that the mass fraction is accurately set as a Dirichlet boundary condition on the droplet surface using the image-point and ghost-cell methodology developed by Mittal et al. [41]. It is shown that the current method achieves a locally and globally second order spatial accuracy while maintaining a sharp representation of the interface. The method is validated against the well known d^2 -law for which the mass fraction value, corresponding to a specific mass transfer number (B_M), is applied as a Dirichlet boundary at the interface. It is also tested for the wet-bulb temperature of a water droplet for a range of ambient conditions and the results are shown to be in good agreement with the psychrometric chart. After that, employing a moving reference frame methodology, the method is applied to study droplet evaporation in a convective environment and the results are compared with the Abramzon-Sirignano (A-S) and the classical models for nearly spherical, moderately deforming and extremely deforming droplet cases. The immersed boundary methodology [41] is also extended to simulate heat and mass transfer from a solid object immersed in a flowing fluid, and the results are found to be in good agreement with the

results reported in the literature.

The rest of the paper is organized as follows. The mathematical formulation of the current study is given in Section 2. Numerical method, including the use of image-point and ghost-cell methodology and the novel front restructuring algorithm, are described in Section 3. The results are presented and discussed in Section 4. Concluding remarks are made in Section 5.

2. Mathematical Formulation

In the front-tracking method, the governing field equations are solved in the entire computational domain using a one-field formulation. The equations can be solved in both conservative and non-conservative forms. In the present study, the non-conservative form is preferred to reduce the inconsistency between the advection schemes used in advancing the interface (thus the material properties) and approximating the convective terms in the momentum equations [9]. In this framework, the incompressible Navier-Stokes equations can be written as [42, 43]:

$$\rho \frac{\partial \mathbf{u}}{\partial t} + \rho [\nabla \cdot (\mathbf{u}\mathbf{u}) - \mathbf{u} (\nabla \cdot \mathbf{u})] = -\nabla p + \rho \mathbf{g} + \nabla \cdot \mu (\nabla \mathbf{u} + \nabla \mathbf{u}^T) + \int_A \sigma \kappa \mathbf{n} \delta(\mathbf{x} - \mathbf{x}_\Gamma) dA, \quad (1)$$

where \mathbf{u} , p and \mathbf{g} denote the velocity vector, the pressure field and the gravitational acceleration, respectively. The density, ρ , and viscosity μ fields vary discontinuously across the phase boundary. The final term on the right-hand side of Eq.(1) represents the body force due to surface tension where σ is the surface tension coefficient, κ is twice the mean curvature and \mathbf{n} is the outward normal vector at the interface. Note that the term, $\rho \mathbf{u} (\nabla \cdot \mathbf{u})$, on the left-hand side of Eq.(1) is needed to account for the surface regression caused by the phase change.

The flow is assumed to be incompressible in both phases. Nevertheless, the mass conservation equation is modified near the interface to account for the volume expansion due to the phase change as [44, 37, 38]:

$$\nabla \cdot \mathbf{u} = \frac{1}{h_{lg}} \left(\frac{1}{\rho_g} - \frac{1}{\rho_l} \right) \int_A \delta(\mathbf{x} - \mathbf{x}_\Gamma) \dot{q}_\Gamma dA, \quad (2)$$

where the delta function indicates that the source term is non-zero at the interface and zero elsewhere, h_{lg} and \dot{q}_Γ represent the latent heat of vaporization and the heat flux per unit time at the interface, respectively. The

subscripts l, g , and Γ , respectively, indicate liquid (droplet) phase, gas phase (ambient fluid) and interface. Taking the evaporation into account, the energy and vapor mass-fraction evolution equations are given by

$$\rho c_p \left(\frac{\partial T}{\partial t} + \mathbf{u} \cdot \nabla T \right) = \nabla \cdot k \nabla T - \int_A \delta(\mathbf{x} - \mathbf{x}_\Gamma) \dot{q}_\Gamma dA, \quad (3)$$

$$\frac{\partial Y}{\partial t} + \mathbf{u} \cdot \nabla Y = \nabla \cdot D_{vg} \nabla Y, \quad (4)$$

where T , c_p , k , Y and D_{vg} are the temperature, the specific heat capacity, the thermal conductivity, the vapor mass-fraction and the vapor mass diffusion coefficient, respectively. The last term on the right hand of Eq. (3) is responsible for the cooling effect due to the evaporation. The heat flux term in Eqs. (3) and (2) is related to the mass flux as $\dot{q}_\Gamma = \dot{m}_\Gamma h_{lg}$. The mass conservation across the interface requires

$$\dot{m}_\Gamma Y_l^\Gamma - \dot{m}_\Gamma Y_g^\Gamma - \rho_g D_{vg} \left(\frac{\partial Y}{\partial n} \right)_\Gamma = 0. \quad (5)$$

Since $Y_l^\Gamma = 1$ for a single-component droplet, Eq. (5) reduces to [37]

$$\dot{m}_\Gamma = \frac{\rho_g D_{vg} \left(\frac{\partial Y}{\partial n} \right)_\Gamma}{1 - Y^\Gamma}, \quad (6)$$

where $\left(\frac{\partial Y}{\partial n} \right)_\Gamma$ is the mass fraction gradient evaluated at the interface in the normal direction. The vapor saturation mass fraction at the interface, Y^Γ , is related to the vapor pressure, P_v^Γ , as

$$Y^\Gamma = \frac{P_v^\Gamma M_v}{P_v^\Gamma M_v + (P_{\text{atm}} - P_v^\Gamma) M_g}, \quad (7)$$

where P_{atm} is the ambient pressure taken here as the atmospheric pressure. The vapor pressure can be obtained from the Clausius-Clapeyron relation as

$$P_v^\Gamma = P_{\text{atm}} \exp \left(-h_{lg} \frac{M_v}{\mathcal{R}} \left(\frac{1}{T_\Gamma} - \frac{1}{T_b} \right) \right), \quad (8)$$

where P_v^Γ is the saturated vapor pressure at the interface temperature T_Γ , T_b is the boiling temperature of the liquid at P_{atm} , M_v and M_g are, respectively, the molar masses of the vapor and gas, and \mathcal{R} is the universal gas constant.

It is further assumed that the material properties remain constant following a fluid particle:

$$\frac{D\rho}{Dt} = 0; \quad \frac{D\mu}{Dt} = 0; \quad \frac{Dk}{Dt} = 0; \quad \frac{Dc_p}{Dt} = 0; \quad \frac{DD_{vg}}{Dt} = 0, \quad (9)$$

where $\frac{D}{Dt} = \frac{\partial}{\partial t} + \mathbf{u} \cdot \nabla$ is the material derivative. The material properties are set in the entire computational domain using an indicator function, I . Letting Ψ denote the set of all material properties, it is computed as

$$\Psi = \Psi_l I(\mathbf{x}, t) + \Psi_g (1 - I(\mathbf{x}, t)), \quad (10)$$

where the indicator function is defined as:

$$I(\mathbf{x}, t) = \begin{cases} 1 & \text{in the droplet phase,} \\ 0 & \text{in the bulk phase.} \end{cases} \quad (11)$$

Note that the vapor mass fraction evolution equation, (i.e., Eq. (4)) is solved only in the bulk phase, so the binary diffusion coefficient, D_{vg} , is defined only outside of the droplet and the associated interfacial boundary condition is enforced using the immersed-boundary method as will be discussed in Section 3.2.

3. Numerical Method

In the finite-difference/front-tracking method [45, 26, 27, 46, 38], a stationary staggered Eulerian grid is used to solve the flow equations fully coupled with the energy and vapor mass-fraction evolution equations while the interface is represented by a separate Lagrangian grid as shown in Fig. 2. In this study, the flow and energy conservation equations are solved in the entire computational domain using a one-field formulation but the species mass-fraction equation is solved only in the ambient fluid and a sharp-interface immersed-boundary method is used to impose the boundary conditions at the interface. The Lagrangian grid (also called front) consists of connected marker points that move with the combination of the local flow velocity interpolated from the neighboring Eulerian grid and the velocity induced by the phase change (see Eq. (13)). A Lagrangian element between two adjacent marker points is called a front element. The Lagrangian grid cast on the Eulerian grid is depicted schematically in Fig. 2a. In the staggered grid arrangement, the velocity components are placed on the cell faces while the

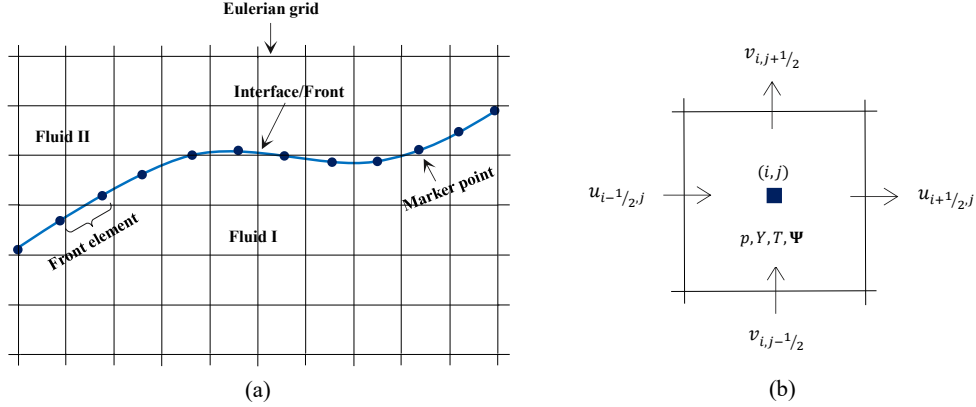


Figure 2: (a) A schematic representation of the Lagrangian grid cast on the stationary Eulerian grid. (b) The staggered grid arrangement used to solve the field equations.

scalar quantities such as pressure, temperature, mass fraction and all the material properties are stored at the cell centers as shown in Fig. 2b.

The Lagrangian marker points are advected in the normal direction as

$$\frac{d\mathbf{x}_\Gamma}{dt} = u_n \mathbf{n}_\Gamma, \quad (12)$$

where \mathbf{x}_Γ is position of marker points, \mathbf{n}_Γ is the outward normal vector and u_n is the normal component of the velocity computed as

$$u_n = \frac{1}{2} (\mathbf{u}_l + \mathbf{u}_g) \cdot \mathbf{n} - \frac{\dot{q}_\Gamma}{2h_{lg}} \left(\frac{1}{\rho_l} + \frac{1}{\rho_g} \right), \quad (13)$$

where \mathbf{u}_l and \mathbf{u}_g are the liquid and gas phase velocities, respectively, and they are evaluated at the interface using one sided interpolation. Full details of the front-tracking method can be found in the review paper by Tryggvason et al. [26] and the book by Tryggvason et al. [9].

3.1. Flow solver

The flow equations are solved on the staggered Eulerian grid using a projection method [47] in which the momentum equation is first written in a semi-discretized form as

$$\rho^n \frac{\mathbf{u}^{n+1} - \mathbf{u}^n}{\Delta t} = \mathbf{A}^n - \nabla p, \quad (14)$$

where Δt is the time step and \mathbf{A} represents the convective, diffusive and body force terms. The superscript n denotes the current time step. This equation is solved in two steps:

$$\rho^n \frac{\mathbf{u}^* - \mathbf{u}^n}{\Delta t} = \mathbf{A}^n, \quad (15)$$

$$\rho^n \frac{\mathbf{u}^{n+1} - \mathbf{u}^*}{\Delta t} = -\nabla p, \quad (16)$$

where \mathbf{u}^* is the unprojected velocity. Taking a divergence of Eq. (16) results in a non-separable Poisson equation for the pressure in the form

$$\nabla \cdot \frac{1}{\rho^n} \nabla p = \frac{\nabla \cdot \mathbf{u}^* - \nabla \cdot \mathbf{u}^{n+1}}{\Delta t}, \quad (17)$$

where $\nabla \cdot \mathbf{u}^{n+1}$ is computed employing Eq.(2) as

$$\nabla \cdot \mathbf{u}^{n+1} = \left[\frac{1}{h_{lg}} \left(\frac{1}{\rho_g} - \frac{1}{\rho_l} \right) \int_A \delta(\mathbf{x} - \mathbf{x}_\Gamma) \dot{q}_\Gamma dA \right]^{n+1}. \quad (18)$$

The pressure Poisson equation (Eq. (17)) is solved using a multigrid method implemented in MUDPACK [48] package as discussed by Tryggvason et al. [26]. Once the pressure field is computed, the velocity field is then corrected to satisfy the mass conservation as

$$\mathbf{u}^{n+1} = \mathbf{u}^* - \frac{\Delta t}{\rho^n} \nabla p. \quad (19)$$

In Eqs. (14)-(17), the spatial derivatives in the convective terms are evaluated using a third-order QUICK scheme [49] while all other spatial derivatives are discretized using central differences on the staggered grid. The surface tension is computed on the interface at the center of the front elements and it is then distributed onto the neighboring Eulerian grid points conservatively in the same manner as described by Tryggvason et al. [26, 9].

The energy and mass-fraction equations are discretized as

$$\frac{T^{n+1} - T^n}{\Delta t} = \left[\frac{1}{\rho c_p} \left(-\mathbf{u} \cdot \nabla T + \nabla \cdot k \nabla T - \int_A \delta(\mathbf{x} - \mathbf{x}_\Gamma) \dot{q}_\Gamma dA \right) \right]^n, \quad (20)$$

$$\frac{Y^{n+1} - Y^n}{\Delta t} = \left[-\mathbf{u} \cdot \nabla Y + \nabla \cdot D_{vg} \nabla Y \right]^n, \quad (21)$$

where the convective terms are approximated using a fifth-order WENO-Z scheme [50] while all other spatial derivatives are evaluated using the central differences on the staggered grid.

The numerical method described above is explicit and only first order in time. However, a formally second-order accuracy can be easily achieved using a predictor-corrector scheme as described by Tryggvason et al. [26]. Although a second-order predictor-corrector scheme is implemented, following Irfan and Muradoglu [38], the first order method is used in the present simulations since the temporal discretization error is generally found to be negligibly small compared to the spatial error owing to a small time step imposed by the numerical stability.

3.2. Interfacial Boundary Conditions: Sharp-Interface Immersed-Boundary Method

The mass-fraction is solved only in the ambient fluid so a special treatment is required to impose the boundary conditions at the interface for Y . In the present work, we use the image point and ghost cell methodology developed by Mittal et al. [41] to accurately impose the Dirichlet boundary condition for the mass fraction at the droplet surface. Note that the same methodology is also used to simulate the flow over a solid sphere in a convective environment as will be discussed in Section 4.2. Following Zolfaghari et al. [51], Eulerian cells cut through by the Lagrangian grid are identified and called ghost cells (GC) as sketched in Fig. 3. Similarly, the vertices of the ghost cells inside the droplet region are called ghost points (GP). Then the boundary intercept (BI) points are determined by drawing a normal line from the associated ghost points to the Lagrangian grid. Finally, the image point (IP) is computed by extending the normal line into ambient fluid by the same distance. After identifying all the BIs and the associated IPs, the vapor mass fraction, Y , is represented in the cell containing an IP by a bilinear interpolant in the form

$$Y(r, z) = a_1 r z + a_2 r + a_3 z + a_4. \quad (22)$$

If the cell containing IP is totally in the ambient fluid domain, the mass fraction at the image point, Y_{IP} , is simply computed by a bilinear interpolation. Otherwise, a linear system is formed to compute the interpolation coefficients as

$$[V] \{A\} = \{Y\}, \quad (23)$$

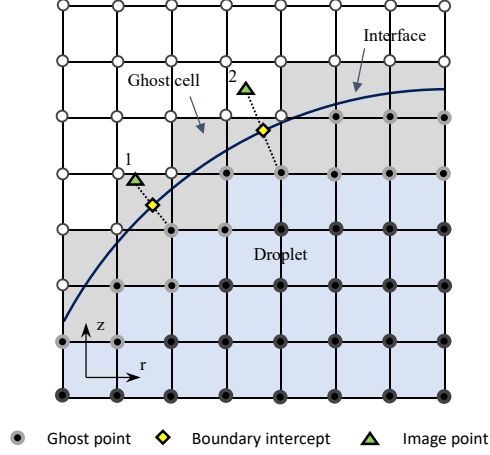


Figure 3: Schematic representation of the sharp-interface immersed-boundary methodology used to impose the species mass boundary condition at the interface. GP, BI and IP denote a ghost cell, a boundary-intercept point, and an image-point, respectively. The image points denoted by 1 and 2 are located partially and totally in the bulk fluid cell, respectively.

where

$$[V] = \begin{bmatrix} r_1 z_1 & r_1 & z_1 & 1 \\ r_2 z_2 & r_2 & z_2 & 1 \\ r_3 z_3 & r_3 & z_3 & 1 \\ r_4 z_4 & r_4 & z_4 & 1 \end{bmatrix}; \{A\} = \begin{Bmatrix} a_1 \\ a_2 \\ a_3 \\ a_4 \end{Bmatrix}; \{Y\} = \begin{Bmatrix} Y_1 \\ Y_2 \\ Y_3 \\ Y_4 \end{Bmatrix}. \quad (24)$$

In Eq. (24), the entries corresponding to a GP are replaced with the boundary conditions. For instance, suppose that the second node is a GP, then we set $r_2 = r_{BI}$, $z_2 = z_{BI}$ and $Y_2 = Y_{BI}$. Note that Y_{BI} is computed at the interface using Eq. (7). Once the interpolation coefficients are determined from Eq. (23), then mass fraction at the image point is simply computed as $Y(r_{IP}, z_{IP}) = a_1 r_{IP} z_{IP} + a_2 r_{IP} + a_3 z_{IP} + a_4$. Finally, the ghost cell value is computed as

$$Y_{GC} = 2Y_{BI} - Y_{IP}. \quad (25)$$

Note that as a fifth-order WENO-Z scheme [50] scheme is used to estimate the convective fluxes in Eq. (4), we employ a larger bandwidth around the interface to locate the ghost and image points as depicted in Fig. 8b. The details of the present sharp-interface immersed-boundary method can be found in Mittal et al. [41] and Zolfaghari et al. [51].

3.3. Species-based evaporation model

The mass flux is computed at the center of the front element from Eq. (6) as

$$\dot{m}_{\Gamma_k} = \left[\frac{\rho_g D_{vg} \left(\frac{\partial Y}{\partial n} \right)_{\Gamma}}{1 - Y^{\Gamma}} \right]_k. \quad (26)$$

Following [37, 38], the mass fraction gradient in the gas phase normal to the interface is approximated as

$$\left(\frac{\partial Y}{\partial n} \right)_{\Gamma} = \frac{1}{\eta h} (Y^+ - Y^{\Gamma}). \quad (27)$$

Referring to Fig. 4, the point (r^+, z^+) is found in the gas phase at a distance ηh from the front element centroid where h is the Eulerian grid spacing and η is a parameter set to 2 in the present study. The normal vectors are easily obtained using smooth tangent vectors that are already calculated using third order Legendre polynomials at each marker point to find the curvature [9] in computing the surface tension. Once (r^+, z^+) is determined, the mass fraction, Y^+ , is approximated using a bi-linear interpolation. Using the mass flux value, the heat flux is computed as

$$\dot{q}_{\Gamma} = h_{lg} \dot{m}_{\Gamma}, \quad (28)$$

which is conservatively distributed onto neighboring Eulerian grid cells to be added as a source term to the energy and continuity equations. The conservation requires

$$\int_{\Delta A} \dot{q}_{\Gamma}(A) dA = \int_{\Delta V} \dot{q}(\mathbf{r}) dV, \quad (29)$$

where \dot{q} is the grid value. Following Tryggvason et al. [26, 9], \dot{q}_{Γ} is smoothed on the Eulerian grid as

$$\dot{q}_{i,j} = \sum_k \dot{q}_{\Gamma}^k w_{i,j}^k \frac{r_k \Delta s_k}{r_{i,j} h^2}, \quad (30)$$

where Δs_k is the length of the front element, r_k is the radial coordinate of the element center, $r_{i,j}$ is the radial position of the respective grid node and $w_{i,j}^k$ is the weight of the Eulerian grid node (i, j) corresponding to the k^{th} element. The weight is calculated using the Peskin's cosine function [52, 26, 38].

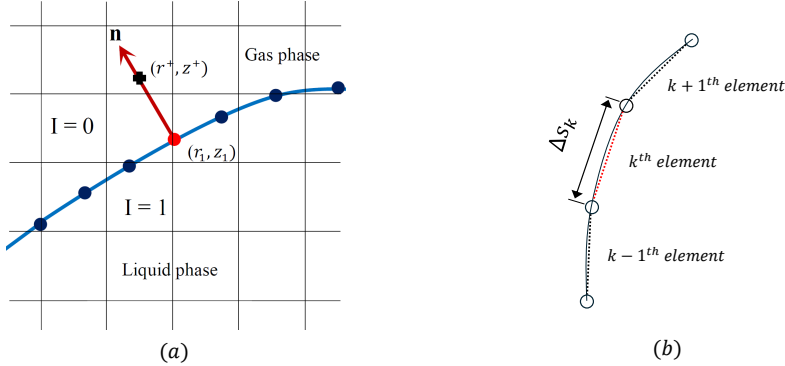


Figure 4: (a) The procedure to find the mass fraction gradient at the interface. (b) A schematic illustration of a front element and its length, Δs_k .

3.4. Restructuring the Lagrangian grid

As the interface continuously deforms and stretches, the Lagrangian grid may become highly non-uniform resulting in an inadequate resolution in some parts while overcrowded in other parts (Tryggvason et al. [26]). It is thus needed to restructure the Lagrangian grid dynamically to keep the front element size nearly uniform throughout the simulation. In the present study, we use a slightly modified version of the original restructuring algorithm developed by Tryggvason et al. [26]. The new procedure is designed to keep the Lagrangian grid uniform throughout a simulation. The algorithm utilizes the same third order Legendre polynomial fit used to compute the interfacial curvature [26]. Starting with the first marker point located on the centerline, we draw a circle of a prespecified radius centered at the marker point and locate the next marker point at the intersection of the circle and the Legendre polynomial, and repeat this procedure until all the marker points are located. This simple algorithm preserves the interface curvature and locates front marker points evenly distributed around droplet perimeter. However, a special treatment may be needed for the second-to-last marker point to avoid the last front element being too small near the centerline. In such cases, the marker point is either removed or repositioned to ensure that the size of the last front element remains within the acceptable threshold. Figure 5 demonstrates the performance of the new front restructuring algorithm for various shapes. The marker points are initialized randomly on the shapes. As seen, the new restructuring algorithm adeptly redistributes the marker points uniformly while preserving the shape of the droplet and its curvature.

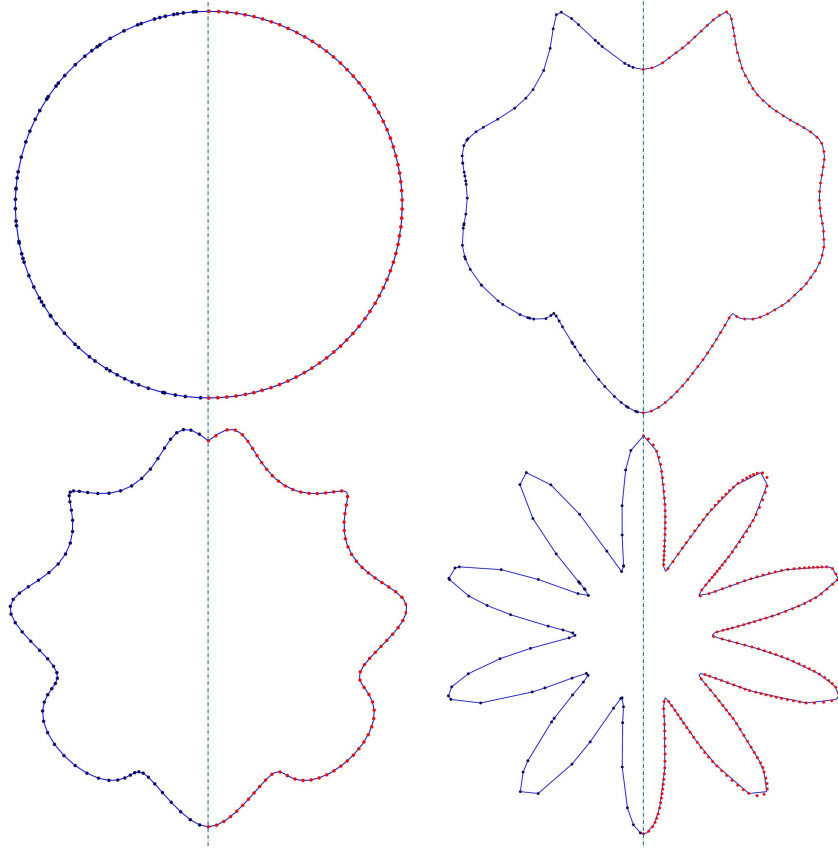


Figure 5: Performance of the new restructuring procedure for the Lagrangian grid. The randomly initialized (black dots on left side) and uniformly restructured (red dots on right side) front marker points for various shapes. The solid blue lines show the pre-specified interfaces.

3.5. Overall solution algorithm

The overall solution algorithm can be summarized as follows:

1. The ghost cells, the boundary intercepts, and the image points are determined using a set of computational geometry operations.
2. The heat flux is computed using Eq. (28) at the n^{th} time step to account for any newly created marker points, and is distributed conservatively on the fixed Eulerian grid.

3. The saturation mass fraction boundary condition is set as a Dirichlet boundary condition on the interface using local temperature interpolated from neighboring Eulerian grid nodes at time level n .
4. The Lagrangian marker points are advected according to Eq.(12) to determine the location of the interface at the new time step, i.e., $x_\Gamma^{n+1} = x_\Gamma^n + \Delta t(u_n n_\Gamma)^n$.
5. The indicator function is computed based on the new location of the marker points and all the material properties are updated according to Eq. (10).
6. The energy and species equations are solved to obtain T^{n+1} and Y^{n+1} .
7. The heat source term at $n+1$ time level is evaluated using the updated energy field and front location, and it is distributed on the fixed grid to be used as a source term in the pressure Poisson equation.
8. The pressure Poisson equation, Eq. (17), is solved, and the velocities at the new time step are corrected.
9. The Lagrangian grid is restructured if needed.

4. Results and Discussion

4.1. Validation of Multiphase Flow Solver

We first perform simulations for a standard test case of a non-evaporating gravity-driven falling droplet [53, 38] to validate the multiphase solver as well as the new Lagrangian grid restructuring algorithm. The computational domain is $5d \times 15d$ and it is resolved by a uniform Cartesian grid of 512×1536 grid cells in the radial and axial directions, respectively. A spherical droplet of diameter d is initialized at $(r_c, z_c) = (0, 13.75d)$ in a rigid cylinder filled with an otherwise quiescent ambient fluid. The no-slip and axisymmetry boundary conditions are applied at the cylinder wall and at the centerline, respectively. Simulations are performed for the density ratio of $\rho_i/\rho_o = 1.15$, the viscosity ratio of $\mu_i/\mu_o = 1$ and the Ohnesorge numbers of $Oh_o = \mu_d/\rho_o d\sigma = 0.05$ and $Oh_i = \mu_i/\rho_i d\sigma = 0.0466$, where subscripts 'o' and 'i' denote the continuous and dispersed phases, respectively. The Eötvös number is defined as $EO = g_z (\rho_i - \rho_o) d^2/\sigma$ and the simulations are repeated for the $EO = 24$, $EO = 48$ and $EO = 96$ cases. The results are shown in Fig. 6 in the non-dimensional form using the length scale d , time scale $\sqrt{d/g_z}$ and velocity scale $\sqrt{dg_z}$. As seen, the present results are in excellent qualitative and quantitative agreement with the published results of Irfan

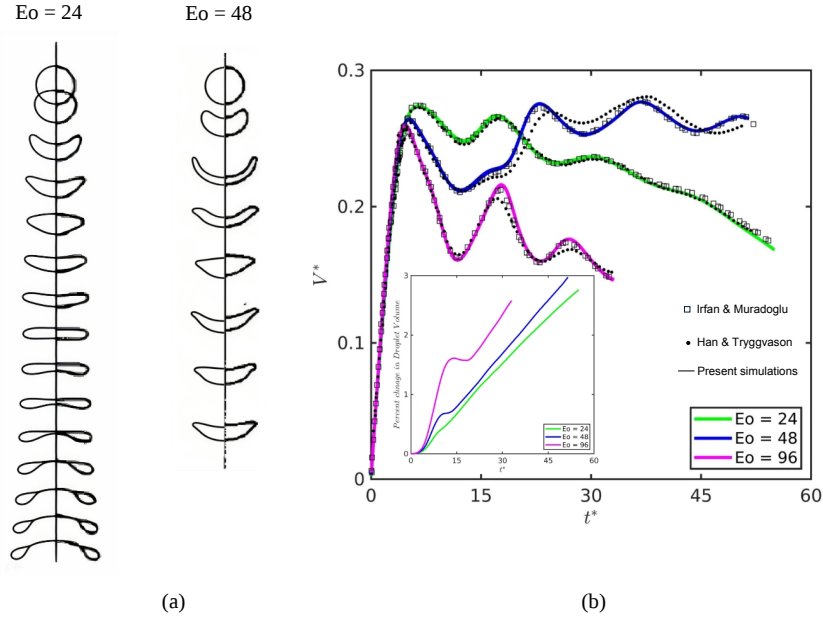


Figure 6: (a) The evolution of the droplet shape for $Eo = 24$ and $Eo = 48$ cases. The present results (left side) are compared with the results of Han and Tryggvason [53] (right side). The time interval between two successive drops in each column is $\Delta t^* = 3.953$ and $\Delta t^* = 5.59$ for $Eo = 24$ and $Eo = 48$, respectively. (b) Comparison of the non-dimensional centroid velocity of a falling droplet with the results of Irfan and Muradoglu [38] and Han and Tryggvason [53] for $Eo = 24, 48$ and 96 . The inset shows the percentage change of the droplet volume during the simulation. ($Oh_o = 0.05, Oh_i = 0.0466, \rho_i/\rho_o = 1.15, \mu_i/\mu_o = 1$, Grid: 512×1536)

and Muradoglu [38] demonstrating the accuracy of the present multiphase solver. Note that the slight discrepancy with the results of Han and Tryggvason [53] is attributed to the lack of resolution in their simulation [53]. Since flow is incompressible, droplet volume change occurs solely due to accumulation of numerical error. The percentage change in the droplet volume is plotted in the inset of Fig. 6b. The volume conservation error is found to be less than 3% for all the cases.

4.2. Mass Transfer from a Solid Sphere

The sharp-interface immersed-boundary (IBM) method is first tested for the case of mass transfer from a solid sphere of diameter d immersed in a uniform ambient flow at moderate Reynolds numbers in the range $50 \leq Re \leq 200$. For this purpose, the IBM method of Mittal et al. [41] is used to

impose the no-slip velocity boundary conditions on the solid sphere surface in addition to the Dirichlet boundary condition applied for the mass transfer. The computational domain is $4d \times 8d$ in the radial and axial directions, respectively. The sphere is held stationary with its center being located at $3d$ from the inlet in the axial direction. A uniform velocity U_∞ is applied at the inlet while constant pressure and zero axial velocity gradient boundary conditions are applied at the outlet. The gradient-free boundary conditions are imposed at the far-field, i.e., at $r = 4d$. The simulations are performed using a 256×512 (coarse), 512×1024 (moderate), and 896×1792 (fine) grid resolutions to demonstrate the grid convergence. Figure 7a illustrates the velocity vectors, streamlines, and the mass fraction field around the sphere at $Re = 200$. As seen, a bound vortex is created in the wake region behind the sphere. The length of the recirculation zone is computed as $L_w = 0.45d, 0.9d, 1.43d$ for $Re = 50, Re = 100$, and $Re = 200$, respectively. These values are in good agreement with the experimental values of 0.48, 0.85 and 1.2 [54, 55] and the numerical results of 0.4, 0.87 and 1.42 [56]. Figure 7b shows the local Sherwood number a function of the angle measured from the stagnation point at the leading edge. The Sherwood number is defined as:

$$Sh = \frac{-2R}{Y^\Gamma - Y_\infty} \left(\frac{\partial Y}{\partial n} \right)_\Gamma, \quad (31)$$

where R is the sphere radius and the gradient term is evaluated in the same way as in Eq. (27). Simulations are repeated for three different grid resolutions and the results are compared with the computational results of Bagchi et al. [57] for $Re = 50$ and $Re = 100$, and of Rodríguez Pérez et al. [58] for $Re = 200$. As seen, the local Sherwood number is captured almost perfectly using the moderate and fine grid resolutions except for the front stagnation point at higher Reynolds numbers. It is worth noting that the mild wiggles observed near the stagnation point are attributed to the rapid circumferential variation of the distance between the boundary intercept points where the boundary conditions are imposed and the corresponding ghost points, as also previously reported by Majumdar et al. [59]. We note that the computations are performed for the Reynolds number up to $Re = 200$ since a vortex shedding is expected to occur behind the sphere for $Re \gtrsim 210$ [57], which cannot be captured by the present axisymmetric simulations.

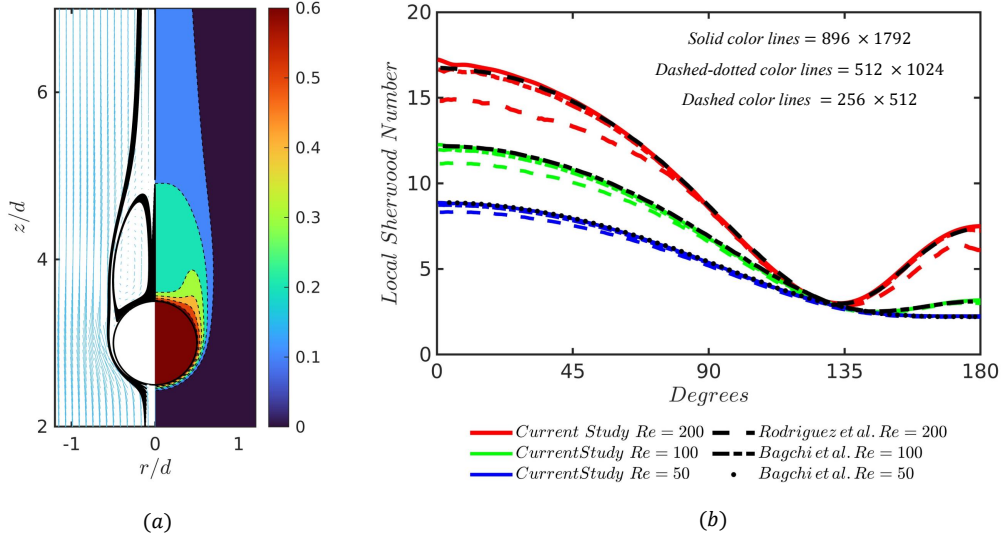


Figure 7: (a) Velocity vectors and streamlines (left portion) and constant contours of species mass fraction (right portion) around a solid sphere at $Re = 200$. (b) Variation of the local Sherwood number. The present results are compared with those of [57] for $Re = 50$ and $Re = 100$, and of [58] for $Re = 200$. Colored dashed, dashed-dotted, and solid lines indicate the present results computed on the grid resolutions of 256×512 , 512×1024 and 896×1792 , respectively. ($Sc = 0.7$.)

4.3. The d^2 -law

We next perform simulations for the well-known test case of a stationary single droplet evaporating in an stagnant ambient air. The initial diameter of the droplet is d_0 . The buoyancy-induced natural convection is neglected. The temporal evolution of the droplet diameter is given by [60, 61]:

$$\frac{dd^2}{dt} = -8 \frac{\rho_g D_{vg}}{\rho_l} \ln(1 + B_M), \quad (32)$$

where ρ_g , ρ_l and D_{vg} denote the gas density, the liquid density and the diffusion coefficient of the vapor in the surrounding air, respectively. The mass transfer potential is defined as $B_M = (Y^\Gamma - Y_\infty)/(1 - Y^\Gamma)$ where Y^Γ and Y_∞ denote the saturation and the far-field vapor mass fractions, respectively. The saturation mass fraction, Y^Γ , is set as a Dirichlet boundary condition on the droplet surface. Simulations are performed for a droplet centered at $(0, 5d_0)$ in a computational domain of $5d_0 \times 10d_0$ using a 256×512 uniform grid resolution in the radial and axial directions, respectively. The time

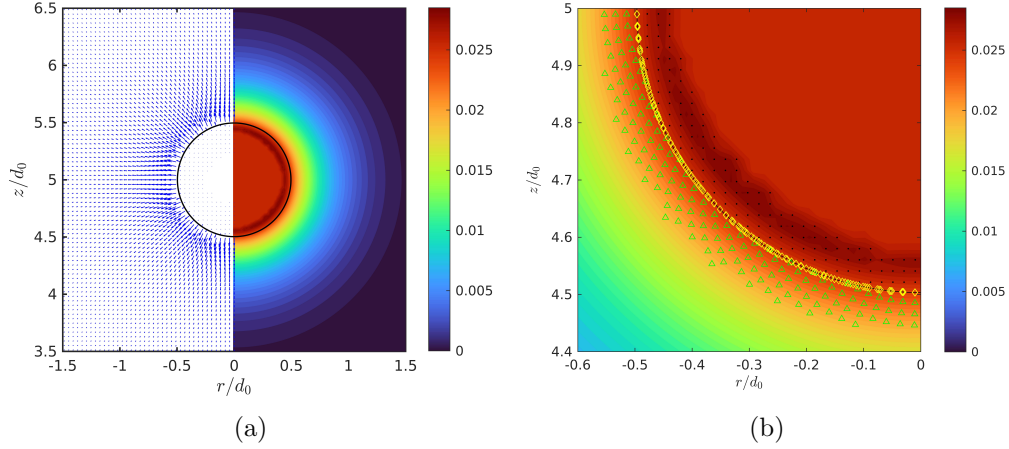


Figure 8: (a) Velocity vectors (left side) and mass fraction field (right side) around an evaporating droplet. (b) An enlarged view illustrating the vapor mass fraction contours as well as distribution of the ghost points (*GP*), boundary intercepts (*BI*) and image points (*IP*) in vicinity of the interface indicated by black dots, yellow diamonds and green triangles, respectively. Constant contours represent the mass fraction field. ($B_M = 0.025$, $t^* = 0.7$).

and length are scaled by d_0 and $\frac{d_0^2}{D_{vg}}$, respectively. Figure 8a illustrates the velocity vectors (Stefan flow) and the constant contours of the vapor mass fraction in the vicinity of the droplet for the case of $B_M = 0.025$ at the scaled time of $t^* = 0.7$. The smooth flow and mass fraction fields qualitatively indicate the accuracy of the numerical method. The enlarged view in Fig. 8b shows the vapor mass fraction as well as the distribution of the ghost cells, the boundary intercepts, and the image points near the interface.

Figure 9a shows the numerical and analytical solutions of time history of $(d/d_0)^2$ in the stagnant conditions for the mass transfer numbers of $B_M = 0.025, 0.05$ and 0.1 . Simulations are repeated using 128×256 , 256×512 and 512×1024 grid resolutions to demonstrate the grid convergence. As seen, the numerical results are in good agreement with the analytical solution and the 128×256 grid resolution is sufficient for the grid convergence. Simulations are also performed to examine effects of the domain size and the results are plotted in Fig. 9b. This figure shows that the numerical results converge to the analytical solution as the domain size increases as expected since the d^2 -law assumes that the droplet evaporates in an unbounded domain. However, increasing the domain size from $5d_0 \times 10d_0$ to $10d_0 \times 20d_0$ does not a significant effect on the overall results for this case. The spatial accuracy

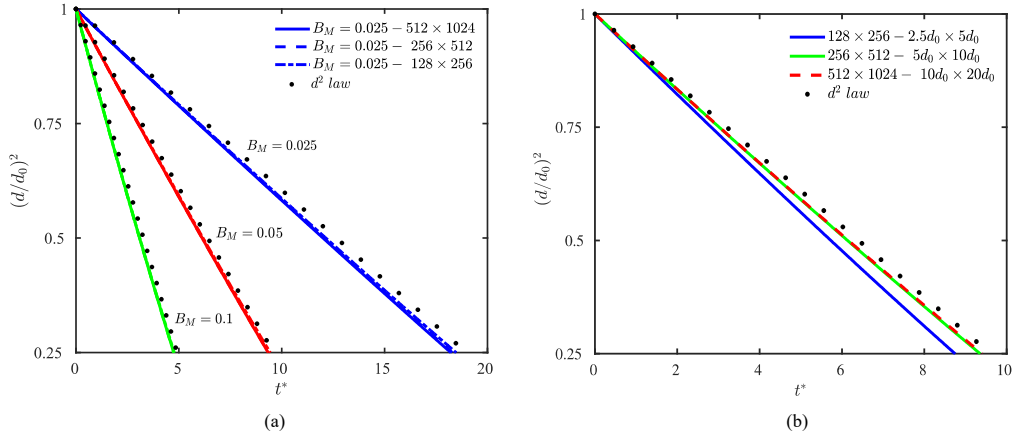


Figure 9: (a) Validation of the numerical method for the d^2 law. The numerical results are compared with the analytical solutions for the mass transfer numbers of $B_M = 0.025$, $B_M = 0.05$, and $B_M = 0.1$. Simulations are performed using 128×256 , 256×512 and 512×1024 grid resolutions to demonstrate the grid convergence. Domain size: $5d_0 \times 10d_0$. (b) The effects of the domain size on the numerical results and comparison with the d^2 -law. The simulations are performed for the domain sizes of $2.5d_0 \times 5d_0$, $5d_0 \times 10d_0$ and $10d_0 \times 20d_0$ using 128×256 , 256×512 , 512×1024 grid resolutions, respectively. ($B_M = 0.05$).

is quantified in Fig. 10. As seen in Fig. 10a, the four finest grids are in the asymptotic range and the nearly linear relationship between $(d/d_0)^2$ and $(h/d_0)^2$ indicates a second order spatial accuracy, which is verified more rigorously in Fig. 10b. Following Muradoglu et al. [62], the error-free values of $(d/d_0)^2$ used to compute the spatial error in Fig. 10b are estimated using the Richardson's extrapolation based on the least-squares fits as $h \rightarrow 0$. The error is then computed as the absolute value of difference between the numerical solution and the predicted spatial error-free value. The linear least-squares fits show that the present numerical method is second order accurate in space. Note that the spatial accuracy was found to be 1.3 for the same case in the previous studies of Irfan and Muradoglu [37, 38] where the mass source term was conservatively distributed outside of the interface using the one-sided adsorption layer method [28, 63]. The results demonstrate that the present method significantly improves the spatial accuracy compared to the one-sided distribution of the mass source term as done in [37, 38].

4.4. Wet-bulb temperature comparison

In this test case, the wet-bulb temperature of a water droplet is computed at various ambient conditions and compared to that of the psychrometric chart

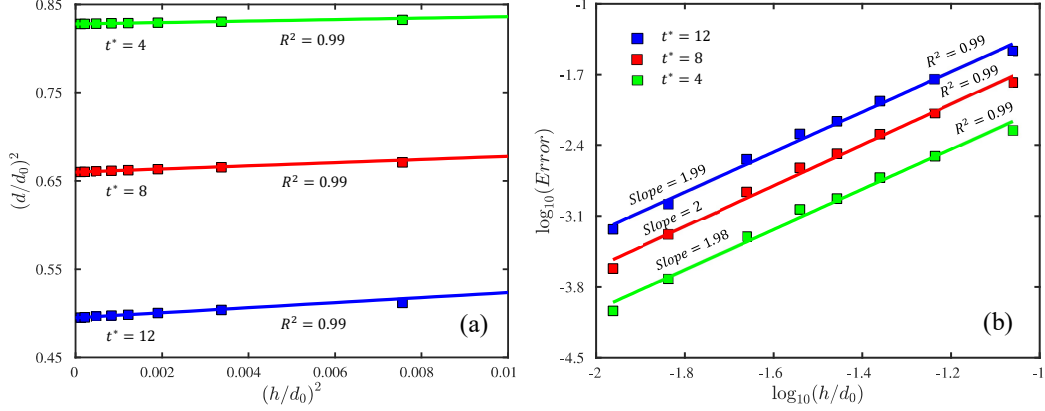


Figure 10: Quantification of the spatial accuracy. The variation of (a) $(d/d_0)^2$ and (b) the spatial error against $(h/d_0)^2$ for a droplet evaporating in stagnant condition. Simulations are performed on the domain size of $5d \times 10d$ for $B_M = 0.025$ using 64×128 , 96×192 , 128×256 , 160×320 , 192×384 , 256×512 , 384×768 and 512×1024 and the results are taken at $t^* = 4$, $t^* = 8$ and $t^* = 12$. The symbols and the solid lines indicate the numerical results and the linear least-squares fits to the numerical values, respectively. Least-squares fitting is done neglecting the values computed on the two coarsest grids.

to demonstrate a proper coupling of the species and temperature fields. A water droplet evaporates solely due to the vapor mass fraction gradient at the interface. As the evaporation proceeds, the temperature at the interface reduces and eventually reaches a steady value called the wet-bulb temperature that is uniquely determined by the relative humidity (RH) and dry-bulb temperature of the ambient air.

In the simulations, a water droplet of initial diameter d_0 is placed centered at $(0, 2.5d_0)$ in a computational domain of $2.5d_0 \times 5d_0$ that is resolved by a 128×256 uniform Cartesian grid. The temperature is initially set to a constant dry-bulb temperature T_g in the entire computational domain. The temperature and vapor mass fraction are fixed at T_g and Y_{vap} as Dirichlet boundary conditions at the domain boundaries where Y_{vap} is computed as $Y_{vap} = \omega_h / (1 + \omega_h)$ with ω_h being the humidity ratio read from a psychrometric chart as a function of dry-bulb temperature and relative humidity. The actual material properties of water and air are used in the simulations except for the water density which is set to $\rho_l = 5\rho_g$. The thermal conductivity of water, k_l , is adjusted to match the physical thermal diffusivity [37]. The results are non-dimensionalized using d_0 and d_0^2/D_{vg} as the length and time scales, respectively. Figure 11 shows the evolution of the tempera-

ture and species fields at various instances for the dry-bulb temperature of $T_g = 323.15$ K and relative humidity of $RH = 10\%$. As the droplet evaporates, the interface temperature decreases and vapor diffuses deeper into the ambient air. This thermal exchange continues until the heat absorbed by the evaporation exactly balances the heat conducted from the ambient air and the water droplet reaches the wet-bulb temperature. Figure 12 shows the temporal evolution of radial temperature profiles along the horizontal center line of the domain width for the cases of $RH = 10\%$ and $RH = 50\%$. As seen, cooling starts at the interface ($r/d_0 = 0.5$) and gradually diffuses into the droplet until the droplet reaches a constant wet-bulb temperature. The computed wet-bulb temperature is compared with the values read from the psychrometric chart in Fig. 13. The wet-bulb temperature is first plotted in Fig. 13a against the relative humidity in the range $10\% \leq RH \leq 80\%$ for the dry-bulb temperature values of 293.15 K and 323.16 K, and then against the dry-bulb temperature in the range $293.1 \text{ K} \leq T_g \leq 323.15 \text{ K}$ for the fixed relative humidity values of 10%, 50% and 80% in Fig. 13b. As seen, the numerical results are in good agreement with the psychrometric chart values in both cases demonstrating accurate coupling of the temperature and vapor mass fraction fields.

4.5. Droplet Evaporation in a Convective Environment

It is computationally not feasible to use the interface-resolved techniques in large scale simulations of evaporating sprays and droplet clouds relevant to industrial applications and environmental flows. Instead, the Lagrangian point particle methods are widely used in modeling the evaporation of sub-grid droplets in such applications [5]. In this approach, the droplets are modeled as Lagrangian point-particles and evaporation models are used to compute the energy and mass transfer rates between droplets and the ambient fluid. Success of such simulations is critically dependent on the accuracy of the low-order evaporation models. A detailed review of the low-order models can be found in the review papers by Faeth [64], Sirignano [65], Law [66] and Sazhin [3, 67].

The interface-resolved simulations can provide indispensable insight into the complex dynamics of droplet evaporation needed for the assessment and improvement/development of the low-order models. Previous studies [17, 20, 68] have predominantly focused on reporting the surface-averaged Sherwood number for a droplet evaporating in a convective environment.

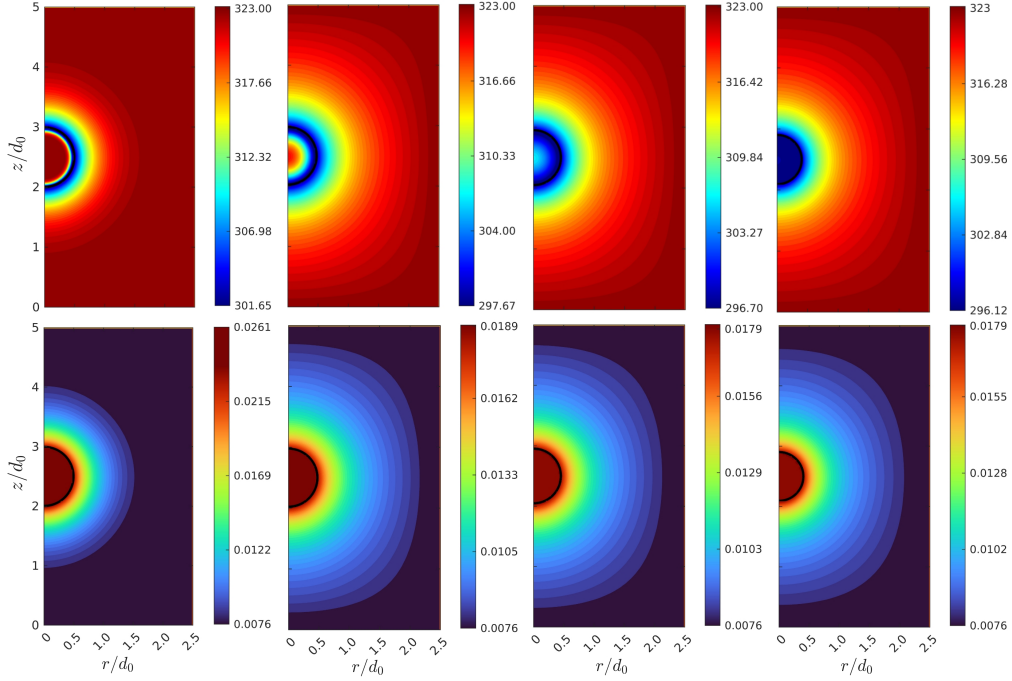


Figure 11: Evolution of temperature (top row) and vapor mass fraction (bottom row) fields for a water droplet evaporating at ambient dry-bulb temperature of 323.15 K and relative humidity of 10% at the non-dimensional times (from left to right) $t^* = 0.02, 0.20, 2.80,$ and 7.91 . (Domain: $2.5d \times 5d$; Grid: 128×256)

However, information regarding distribution of the Sherwood number at interface, particularly for a deforming droplet, is very scarce. Employing the IB/FT method, we demonstrate how droplet deformation can fundamentally alter the distribution of Sherwood number. In this section, the present numerical method is applied to simulate a droplet evaporating in a convective environment and the results are compared with the analytical models for the mass transfer number in the range $1 \leq B_M \leq 15$.

To mimic the evaporation of a droplet in a convective environment, the center of mass of the droplet is fixed in the space using a moving reference frame (MRF) methodology, and the momentum equation is modified accordingly to account for the acceleration of the reference frame [69]. In the experimental studies, the droplet is usually deposited on a fiber to keep it fixed in space in a flowing ambient fluid [70, 71, 72, 73]. However, in the real-world applications such as spray evaporation and cloud formation,

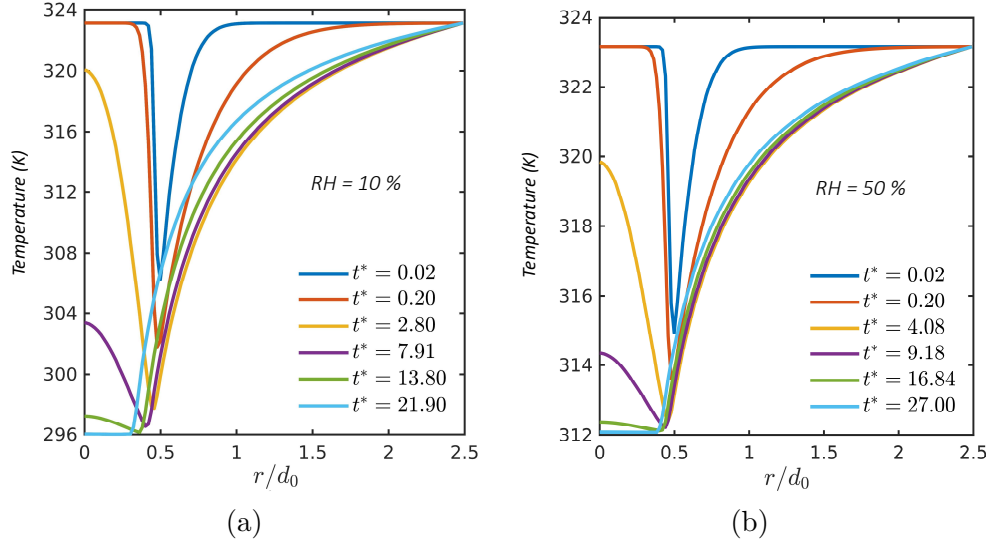


Figure 12: Temperature profiles plotted along the centerline of the droplet in the radial direction at various non-dimensional times. Dry bulb temperature is 323.15 K. Relative humidity is (a) 10% and (b) 50%. (Domain: $2.5d \times 5d$; Grid: 128×256)

droplets can freely translate and deform in the ambient fluid flow. Therefore, employing a moving reference frame provides a more relevant framework to study droplet evaporation in a convective environment. Accounting for the acceleration of the MRF, the modified momentum equation can be written in the non-conservative form as [69]

$$\rho \frac{\partial \mathbf{u}_{rel}}{\partial t} + \rho [\nabla \cdot (\mathbf{u}_{rel} \mathbf{u}_{rel}) - \mathbf{u}_{rel} (\nabla \cdot \mathbf{u}_{rel})] = -\nabla p + \rho (\mathbf{g} + \mathbf{a}_{MRF}) + \nabla \cdot \mu (\nabla \mathbf{u}_{rel} + \nabla \mathbf{u}_{rel}^T) + \int_A \sigma \kappa \mathbf{n} \delta(\mathbf{x} - \mathbf{x}_\Gamma) dA, \quad (33)$$

where \mathbf{u}_{rel} is the relative velocity and \mathbf{a}_{MRF} is the acceleration needed to hold the centroid of the droplet fixed with respect to the computational domain. In the present study, the procedure proposed by Rusche [69] is used to compute \mathbf{a}_{MRF} .

We consider a deformable droplet whose center is fixed in the space in a flowing ambient fluid as sketched in Fig. 14. The ambient flow is uniform far from the droplet and its velocity is U_∞ . The droplet is initially spherical with a diameter of d_0 and its center is located at the axial distance of $2.5d_0$ from the inlet. The computational domain is $4d_0 \times 8d_0$ and it is resolved by a

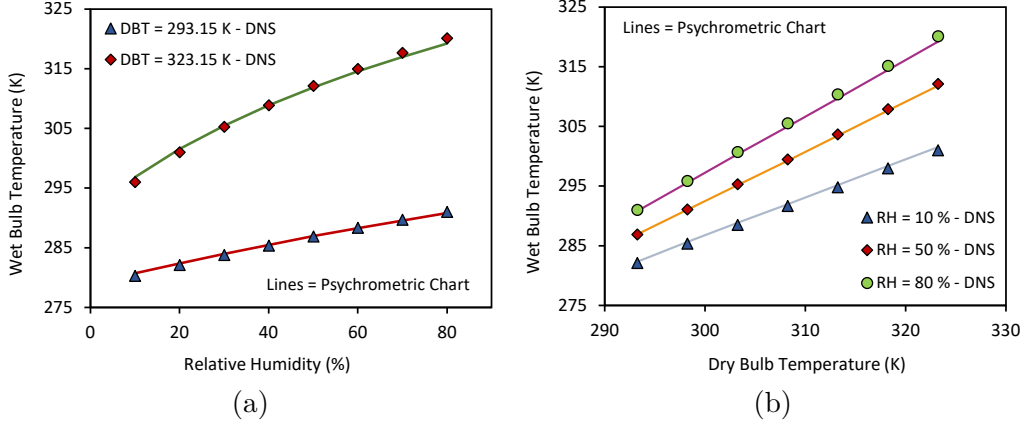


Figure 13: (a) Variation of the wet-bulb temperature with respect to the relative humidity at fixed dry-bulb temperatures of 293.15 K and 323.15 K. (b) Effect of increasing dry-bulb temperature at a fixed relative humidity of 10%, 50%, and 80%. (Domain: $2.5d \times 5d$; Grid: 128×256)

512×1024 uniform Cartesian grid in the radial and axial directions, respectively. In all the simulations, a uniform velocity U_∞ is specified at the inlet section corresponding to the specified Reynolds number while the symmetry and full-slip boundary conditions are applied at the left (centerline) and the right (far-field) boundaries. The Dirichlet mass fraction boundary condition, corresponding to a specific mass transfer number (B_M), is applied on the droplet surface and the vapor mass fraction is set to zero at the inlet, i.e., the gas is dry. The gravitational effects are neglected to facilitate a direct comparison with the evaporation models.

The relevant non-dimensional parameters for this study are defined as

$$Re = \frac{\rho_g U_\infty d_0}{\mu_g}, \quad We = \frac{\rho_g U_\infty^2 d_0}{\sigma}, \quad Sc = \frac{\mu_g}{\rho_g D_{vg}}, \quad (34)$$

where Re , We and Sc are the Reynolds, Weber and Schmidt numbers, respectively. The Reynolds and Schmidt numbers are fixed at $Re = 100$ and $Sc = 0.7$ in all the results presented here. Simulations are carried out for three different Weber numbers representing a nearly spherical ($We = 0.65$), a moderately deformable ($We = 6.5$) and a highly deformable ($We = 13$) cases. The viscosity and density ratios constitute the other relevant non-dimensional numbers and they are fixed at $\mu_l/\mu_g = 15.34$, and $\rho_l/\rho_g = 25.75$, respectively. Note that the subscripts 'l' and 'g' denote the properties of the

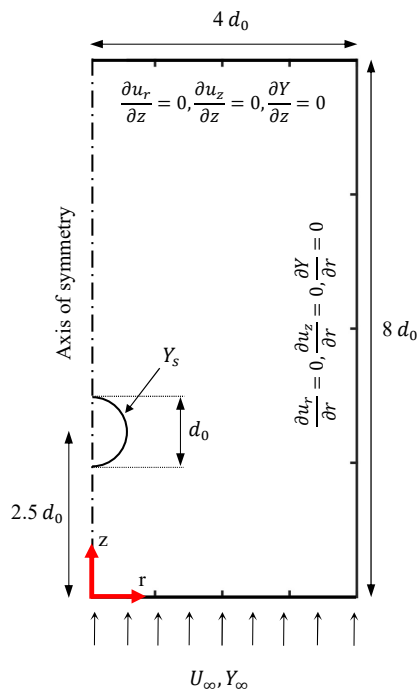


Figure 14: Sketch of the computational domain and the boundary conditions used for simulation of droplet evaporation in a convective environment.

droplet liquid and the ambient gas, respectively.

Simulations are first performed to demonstrate grid convergence and to quantify the spatial accuracy of the numerical method for this challenging test case. For this purpose, the effect of grid refinement on the local Sherwood number is considered. Figures 15a and 15c show the distribution of local Sherwood number computed at $t^* = 5$ using various grid resolutions in the range between 80×160 and 768×1536 for a nearly spherical ($We = 0.65$) and a highly deformable ($We = 13$) cases. As seen, the difference between the results obtained on successive grid resolutions decreases with grid refinement, indicating a grid convergence. The spatial accuracy is quantified in Figs. 15b and 15d where the local Sherwood number is plotted against the square of the normalized grid size $(h/d_0)^2$ at various angles indicated by the dotted vertical lines in Figs. 15a and 15c. In these figures, symbols denote numerical values while solid lines are linear least-squares fits to the numerical data. Note that only the numerical values obtained on the grid resolutions in the asymptotic range are used in the linear least-squares fits. The nearly

linear relationship between the numerical values and linear least-squares fits indicates that the numerical method is second order accurate in space, which constitutes a major advantage of the present hybrid method compared to the method developed by Irfan and Muradoglu [37, 38] where the spatial accuracy was only first order. Figure 15 shows that the 512×1024 grid resolution is sufficient to reduce the spatial error below 0.5% and 7% for nearly spherical ($We = 0.65$) and highly deformable ($We = 13$) cases, respectively. Therefore, this grid resolutions is used in all the subsequent simulations. The larger numerical error for the most deformable case is due to a significantly fewer number of grid points inside the deformed droplet compared to that in the nearly spherical one. For instance, number of grid points along the axis of symmetry inside the droplet is 130 and 40 for the nearly spherical ($We = 0.65$) and the highly deformed ($We = 13$) cases, respectively, i.e., the nearly spherical droplet is about three times better resolved.

Figure 15 shows that the variation of the local Sherwood number over the deformed droplet ($We = 13$) is fundamentally different than that of the nearly spherical one ($We = 0.65$). For instance, the local Sherwood number becomes maximum at the centerline on the leading edge for the nearly spherical droplet while it occurs in the shoulder region of the deformed droplet. This marked difference clearly demonstrates the importance of droplet deformation that is totally ignored in the commonly used low-order evaporation models.

The density ratio is of order of 1000 in actual spray combustion simulations but the well-known inconsistency in the advection schemes used to advect the density and the momentum causes numerical difficulties in the present front-tracking method at very high density ratios [9]. Therefore the density ratio is usually limited to $\rho_l/\rho_g \leq 40$. Olgac et al. [74] and Tasoglu et al. [75] have shown that the results are not affected significantly when the density ratio is further increased beyond $\rho_l/\rho_g = 20$. Simulations are performed for the range of density ratio between $10 \leq \rho_l/\rho_g \leq 40$ to examine sensitivity of results to density ratio and to determine the density ratio beyond which the results are not affected significantly. The other parameters are fixed at $Re = 100$, $Sc = 0.7$, $We = 0.65$, $B_M = 2$ and $\mu_l/\mu_g = 15.34$. The results are shown in Fig. 16b. As seen, the results are insensitive to variation in the density ratio beyond $\rho_l/\rho_g \geq 25.75$. Thus, the density ratio is kept constant at $\rho_l/\rho_g = 25.75$ in all the simulations presented in this section unless specified otherwise.

After demonstrating grid convergence and insensitivity to the density ra-

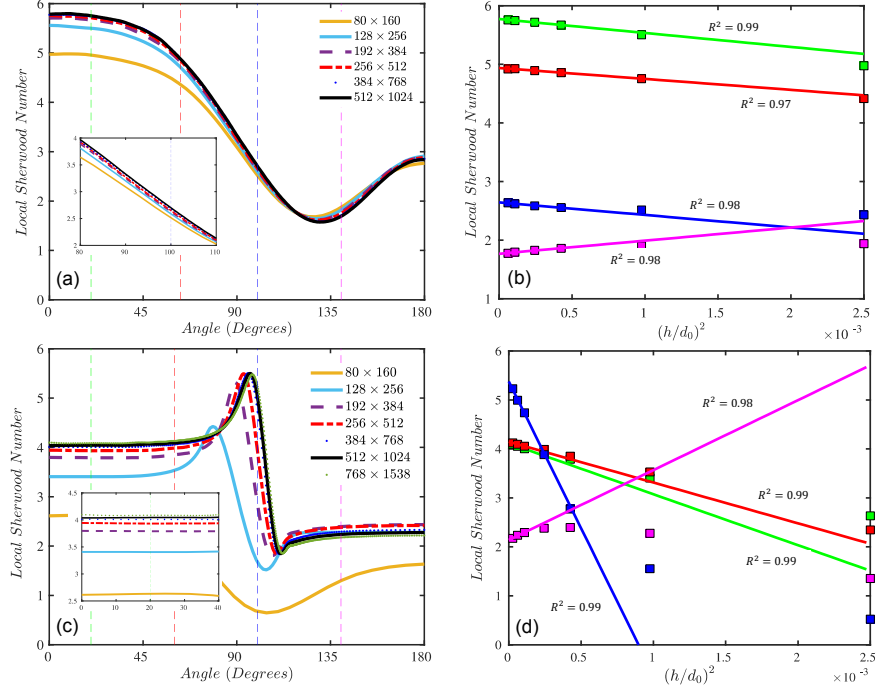


Figure 15: Local Sherwood number computed over (a) nearly spherical ($We = 0.65$) and (c) highly deformable ($We = 13$) droplets for $Re = 100$ and $B_M = 2$ at $t^* = 5$. Grid resolutions: 80×160 , 128×256 , 192×384 , 256×512 , 384×768 , 512×1024 , and 768×1536 . Quantification of the spatial accuracy for (b) the nearly spherical ($We = 0.65$) and (d) the highly deformable ($We = 13$) droplets.

tio, the numerical method is applied to simulate non-evaporating and evaporating droplets for $We = 0.65$, 6.5 , and 13 to show its capability in resolving evaporation of nearly spherical and highly deformable droplets in a convective environment. It is emphasized here that the term of “*non-evaporating droplet*” is used here to refer to the case that the mass transfer from the droplet does not induce any Stefan flow, i.e., the Stefan flow is switched off manually to demonstrate its sole effect on the flow field and the mass transfer from the droplet. Figure 17 illustrates the velocity vectors, streamlines and mass fraction field around non-evaporating (i.e., no Stefan flow) and evaporating ($B_M = 2$) droplets at $Re = 100$. As seen, a flow separation occurs in all the cases creating a recirculation zone behind the droplet that broadens as the droplet deformation (i.e., We) increases [76]. In the evaporating cases, the streamlines are pushed away from the droplet surface due to the Ste-

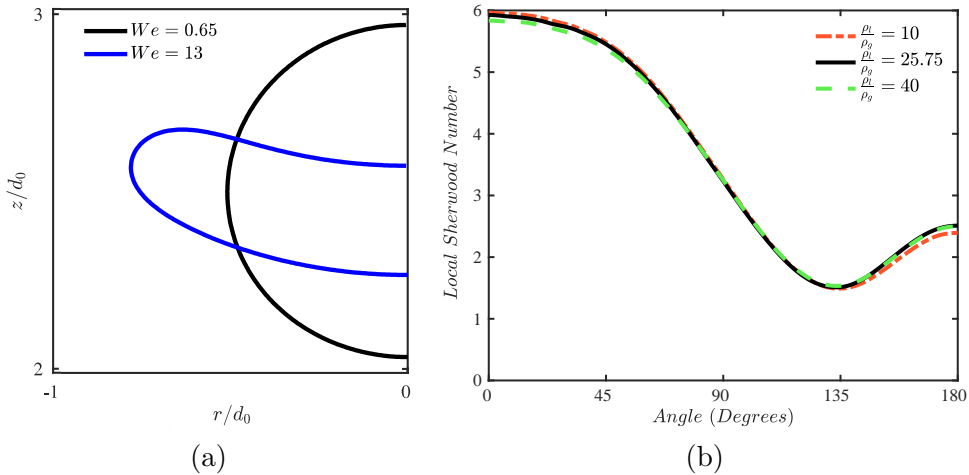


Figure 16: (a) Droplet shapes for the nearly spherical ($We = 0.65$) and highly deformable ($We = 13$) cases at $t^* = 5$. (b) Effect of density ratio on Sherwood number distribution for the $We = 0.65$ case. ($Re = 100$, $Sc = 0.7$, $B_M = 2$. Grid: 512×1024).

fan flow, resulting in a thickened boundary layer that leads to an early flow separation and a broader recirculation zone compared to the corresponding non-evaporating cases. In addition, the front and back stagnation points are detached from the surface of the droplet for the same reason in the evaporating cases. As can be seen in Figs. 17(b) and 17(c), the Stefan flow also slightly influences deformation of droplet.

To better show the effects of the Stefan flow, further simulations are performed for the moderately deforming droplet case of $We = 6.5$ at various evaporation intensities, i.e., at $B_M = 5, 10$ and 15 , which can be relevant in high temperature spray combustion applications. The results are plotted in Fig. 18. As the Stefan flow intensifies with increasing B_M , the streamlines are pushed further away from the droplet interface and the recirculation zone gets enlarged. This figure clearly shows the importance of the Stefan flow which can be as large as that of the mean flow and modify the entire flow field around the droplet. These results also indicate that the present numerical method can successfully simulate the evaporating droplets with high evaporation intensities.

Finally, we compare the interface-resolved simulation results with the commonly used low-order evaporation models, i.e., the classical [3] and Abramzon and Sirignano (A-S) [77, 78] models. Both models ignore droplet deformation and assume that droplet remain spherical during the entire evapora-

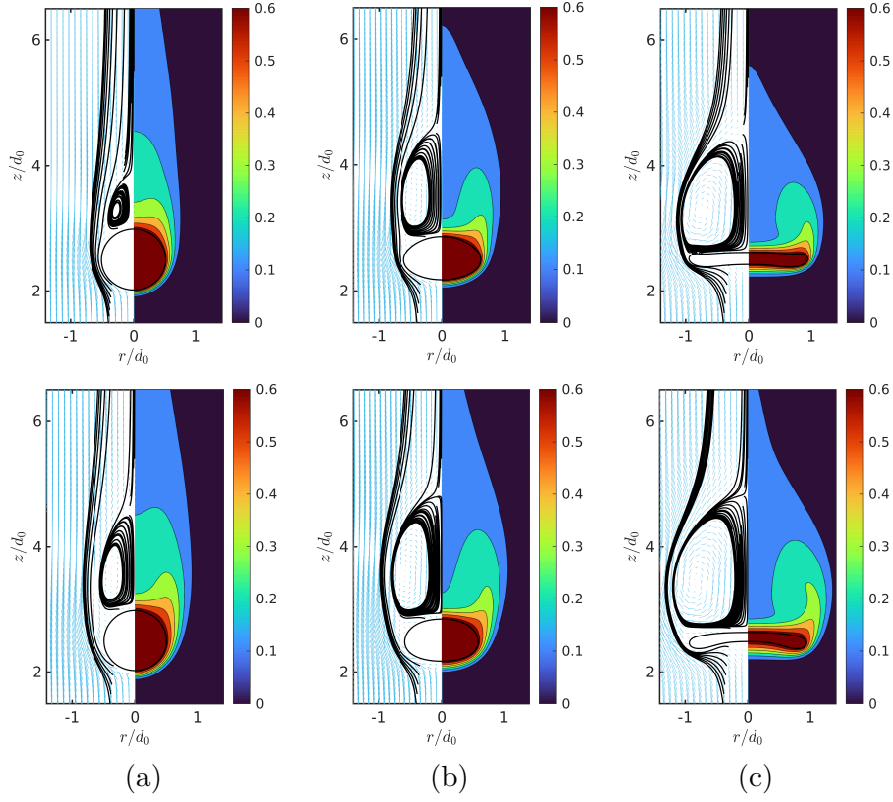


Figure 17: Effects of droplet deformability. Velocity vectors and streamlines (left portion) and vapor mass-fraction field (right portion) are shown for the non-evaporating (no Stefan) (top row) and evaporating ($B_M = 2$) (bottom row) cases at $t^* = 9$. Weber numbers are 0.65 (a), 6.5 (b), and 13 (c) from left to right. The other parameters are $Re = 100$, $\rho_l/\rho_g = 25.75$, $\mu_l/\mu_g = 15.34$ and $Sc = 0.7$. Color bars indicate the values of mass fraction. (Domain: $4d_0 \times 8d_0$; Grid: 512×1024).

tion process. The classical model takes into account effect of the Stefan flow on mass transfer rate from evaporating droplets [3] but ignores the boundary layer thickening caused by the surface blowing. According to the classical model, the Sherwood number is given by

$$Sh = Sh_0 \frac{\ln(1 + B_M)}{B_M}, \quad (35)$$

where Sh_0 is the Sherwood number for the non-vaporizing spherical particle and it is usually estimated using the correlations obtained for the mass transfer from a solid sphere. For instance, the Frossling correlation [79] is

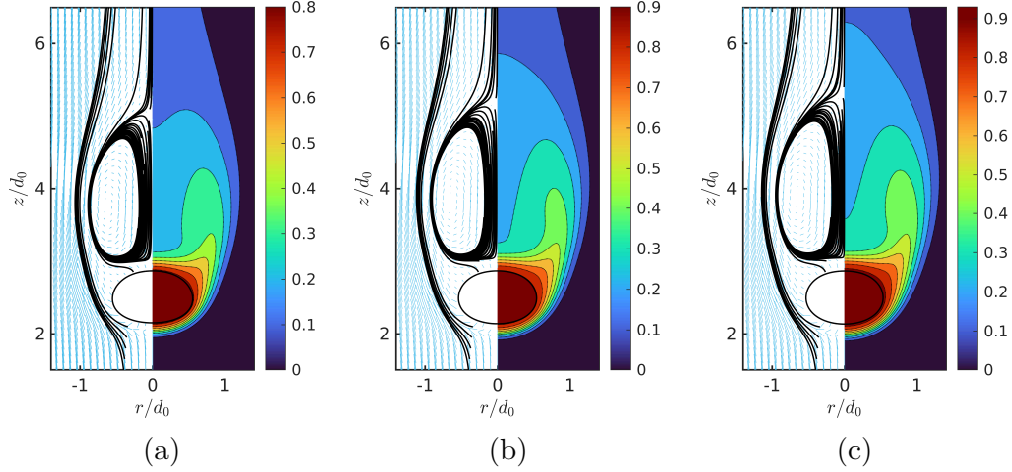


Figure 18: Effects of evaporation intensity. Velocity vectors and streamlines (left portion) and vapor mass-fraction field (right portion) around a moderately deformable evaporating droplet at $Re = 100$, $t^* = 9$, and mass transfer numbers of (a) $B_M = 5$, (b) 10, and (c) 15. Color bars indicate the value of vapor mass-fraction. (Domain: $4d_0 \times 8d_0$; Grid: 512×1024).

widely used in spray simulations and it is given by

$$Sh_0 = 2 + 0.552 Re^{\frac{1}{2}} Sc^{\frac{1}{3}}. \quad (36)$$

Abramzon and Sirignano [77, 78] proposed a modification to the classical model to account for the effects of boundary layer thickening due to the surface blowing of the Stefan flow. They took into account the adverse effect of Stefan flow on the Sherwood number by approximating the droplet as a collection of evaporating wedges. They found that the correction factor is essentially dependent on the mass transfer number, and proposed the following correction to quantify its effect on the Sherwood (or Nusselt) number

$$Sh = 2 + \frac{Sh_0 - 2}{F_M}, \quad (37)$$

$$F_M = (1 + B_M)^{0.7} \frac{\ln(1 + B_M)}{B_M}$$

Note that the Frossling correlation (i.e., Eq. (36)) gives an average value of the Sherwood number for a spherical particle but it does not provide any information for the local mass transfer rate. Thus, the local Sherwood number, i.e., the distribution of Sh_0 , is directly obtained from the sharp-interface immersed boundary method simulations, and it is used in evaluating the classical and Abramzon and Sirignano models in the present study.

Figures 19a and 19b, respectively, show the variation of the local Sherwood number over a nearly spherical and a moderately deforming evaporating droplet for the range of mass transfer numbers between $1 \leq B_M \leq 15$ at $t^* = 9$. The numerical results are compared with the Abramzon-Sirignano model where the local Sh_0 is taken from separate the sharp-interface immersed-boundary simulations performed for the mass transfer from a solid sphere of the initial droplet radius. Note that the change in droplet diameter is neglected in evaluating Sh_0 since the evaporative mass loss causes less than 5% decrease in droplet diameter until $t^* \leq 9$, resulting in less than 1.75% reduction in the surface-averaged Sherwood number. In addition, as mentioned before, the Stefan flow is switched off in the case of *No Stefan Flow* plotted in Fig. 19 to demonstrate its sole effect. As seen, the Abramzon-Sirignano model agrees reasonably well with the numerical results for the nearly spherical droplet case especially in the leading edge until a flow separation occurs. In the wake region, it generally underpredicts the mass transfer rate. As droplet undergoes a significant deformation, its performance deteriorates quickly resulting in a qualitatively inaccurate prediction of local Sherwood number all over the droplet especially at smaller mass transfer numbers.

Figure 19c illustrates the temporal variation of the surface-averaged droplet Sherwood number computed for three different Weber numbers of $We = 0.65, 6.5,$ and 13 , in comparison with the Abramzon-Sirignano and the classical models. Note that, in this figure, Sh_0 is evaluated using the Frossling correlation based on the instantaneous Reynolds number of the moderately deforming droplet ($We = 6.5$) for each mass transfer number. The equivalent droplet diameter is used in evaluating the Sherwood number for deformable cases. We also note that the maximum reduction in the droplet diameter is about 7.3% at the end of the simulation for the highly deformable case at $B_M = 15$ in Fig. 19c. According to the Frossling correlation, this reduction results in a maximum decrease of 2.6% in the Sherwood number. Figure 19c shows that the Abramzon-Sirignano model outperforms the classical model for all the mass transfer numbers. As seen, the Abramzon-Sirignano model slightly under-predicts while the classical model considerably over-predicts the average Sherwood number. The discrepancy between the Abramzon-Sirignano and DNS is consistent with the analysis shown in Figs. 19a and 19b.

Figure 19c also reveals the transient effect of droplet deformability on the surface-averaged Sherwood number. Note that Sh_{ave} remains about the same for all B_M values regardless of the droplet Weber number until the droplet

undergoes a significant deformation, i.e., until $t^* = 1.2$. Then, the effects of droplet deformability becomes visible in the surface-averaged Sherwood number. It is interesting to observe that the surface-averaged Sherwood number becomes very similar for the nearly spherical and moderately deformed cases when a quasi steady-state is attained. For instance, at $B_M = 1$, the averaged Sherwood number is found to be $Sh_{ave} = 6.77$ and $Sh_{ave} = 6.89$ for the nearly spherical and the moderately deformed cases, respectively. The time evolution of Sh_{ave} is also similar for these cases. However, in the highly deformed droplet case, Sh_{ave} deviates considerably and the difference becomes as large as 8%. More importantly, the time evolution is also qualitatively different in this case. This figure also shows that the Abramzon-Sirignano model is very successful in predicting the average Sherwood number especially in the nearly spherical case. It is interesting to observe that, in spite of the qualitative differences in the local Sherwood number distributions as shown in Fig. 19b, there is much better agreement between the fully-resolved results and the Abramzon-Sirignano model predictions for the average Sherwood numbers. The increased surface area of the deformed droplet leads to an overall higher mass transfer rate as also reported by Setiya and Palmore [76]. However, despite this over all increase, the surface-averaged Sherwood number appears to be lower for the highly deformed case as demonstrated in Fig. 19b.

5. Conclusions

This study presents a novel hybrid sharp-interface immersed-boundary/front-tracking method for interface-resolved simulations of a droplet evaporation in incompressible multiphase flows. A distinctive feature of this work is the incorporation of an image point and ghost cell methodology into the front-tracking framework to achieve a second order spatial accuracy for the mass transfer at the interface. The methodology is also used successfully to impose the no-slip boundary conditions on a solid sphere.

The multiphase flow solver is validated for a falling droplet case. Then the numerical method is applied to simulate a single phase flow over a solid sphere in a uniform ambient flow to show the accuracy of the sharp-interface immersed-boundary method. The results are found to be in excellent agreement with the published numerical results for the both cases.

The evaporation model is first validated for the classical d^2 -law test case and the numerical results are found to be in excellent agreement with the

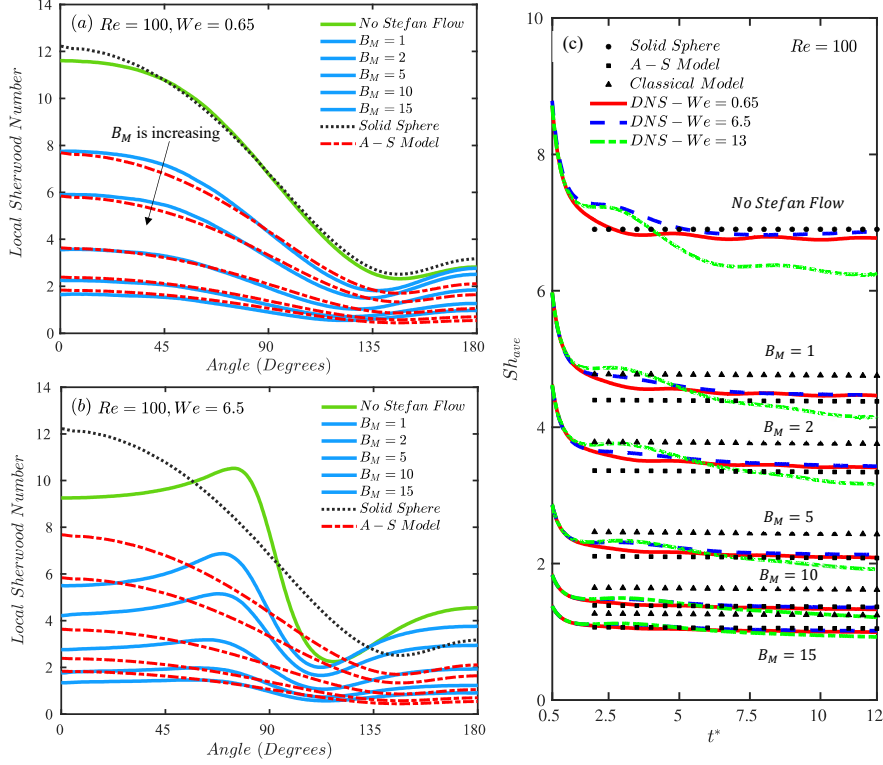


Figure 19: Interface-resolved simulation results for the local Sherwood number over (a) a nearly spherical and (b) a moderately deformable droplet in comparison with the Abramzon-Sirignano model ($Re = 100$ and $t^* = 9$). (c) Temporal evolution of the interface-resolved surface-averaged Sherwood number for a nearly spherical ($We = 0.65$), a moderately deformable ($We = 6.5$), and a highly deformable ($We = 13$) droplet at $Re = 100$. The numerical results are compared with the classical and Abramzon-Sirignano models. The Sherwood number computed for a solid sphere is also shown on the right.

analytical solution. It is demonstrated that the method is grid-convergent and second-order accurate in space, surpassing the previous front-tracking method that employs an absorption layer to impose the mass transfer boundary conditions indirectly and results in only a first order spatial accuracy [37, 38]. The method is then applied to simulate the wet-bulb temperature of a water droplet under various ambient conditions to show its performance for two-way coupling of species and energy fields, and the numerical results are found to be in good agreement with the psychrometric chart values.

The method is finally applied to study droplet evaporation in a convective

environment and the results are compared with the classical and Abramzon-Sirignano evaporation models. Using a moving reference frame methodology, simulations are performed for a nearly spherical, a moderately deformable and a highly deformable droplet cases to show the effects of droplet deformation on evaporation. The Reynolds number is kept constant at $Re = 100$ but the mass transfer number is varied in the range of $1 \leq B_M \leq 15$ to show the ability of the numerical method to simulate slowly and rapidly evaporating cases. It is demonstrated that the numerical method is grid convergent and it is second order accurate in space for this more challenging test case. It is found that a flow separation occurs on the shoulder of the droplet and a large recirculation zone is created behind the droplet at this Reynolds number. The Stefan flow thickens the boundary layer and results in an earlier flow separation and a larger recirculation zone compared to the corresponding non-evaporating case. This effect is amplified as the mass transfer number is increased. The numerical results are compared with the classical and Abramzon-Sirignano models in terms of the local and surface-averaged Sherwood numbers. It is found that the Abramzon-Sirignano model performs well in predicting the Sherwood number on the leading edge of the droplet but its performance deteriorates significantly in the recirculation zone behind the droplet, i.e., after the separation point. It is generally found that the low-order models fall short in accurately predicting the local Sherwood number in the wake region.

The results clearly demonstrate that the present hybrid method is grid convergent with a second order spatial accuracy and it is well suited for interface-resolved simulation of droplet evaporation even in largely deforming and rapidly evaporating conditions in a strong convection relevant to spray combustion applications.

Acknowledgment

We acknowledge financial support from the Scientific and Technical Research Council of Turkey (TUBITAK) [Grant Number 121M361].

CRedit authorship contribution statement

F. Salimezhad: Conceptualization, methodology, investigation, software, validation, formal analysis, visualization, writing – original draft. **H. Turkeri:** Project administration, funding acquisition, investigation, review

& editing. **I. Gokalp:** Funding acquisition, investigation, review & editing. **M. Muradoglu:** Conceptualization, software, resources, investigation, writing – review & editing, supervision, project administration, funding acquisition.

declaration of competing interest

The authors declare that they have no known competing financial interests or personal relationships that could have appeared to influence the work reported in this paper.

References

- [1] T. Dauxois, T. Peacock, P. Bauer, C. P. Caulfield, C. Cenedese, C. Górlé, G. Haller, G. N. Ivey, P. F. Linden, E. Meiburg, N. Pinardi, N. M. Vriend, A. W. Woods, Confronting grand challenges in environmental fluid mechanics, *Phys. Rev. Fluids* 6 (2021) 020501. URL: <https://link.aps.org/doi/10.1103/PhysRevFluids.6.020501>. doi:10.1103/PhysRevFluids.6.020501.
- [2] R. Mittal, R. Ni, J.-H. Seo, The flow physics of covid-19, *Journal of Fluid Mechanics* 894 (2020) F2. doi:10.1017/jfm.2020.330.
- [3] S. S. Sazhin, Advanced models of fuel droplet heating and evaporation, *Progress in energy and combustion science* 32 (2006) 162–214.
- [4] M. Birouk, I. Gokalp, Current status of droplet evaporation in turbulent flows, *Progress in Energy and Combustion Science* 32 (2006) 408–423. URL: <https://www.sciencedirect.com/science/article/pii/S0360128506000220>. doi:<https://doi.org/10.1016/j.pecs.2006.05.001>.
- [5] P. Jenny, D. Roekaerts, N. Beishuizen, Modeling of turbulent dilute spray combustion, *Progress in Energy and Combustion Science* 38 (2012) 846–887. URL: <https://www.sciencedirect.com/science/article/pii/S0360128512000445>. doi:<https://doi.org/10.1016/j.pecs.2012.07.001>.

- [6] C. C. Wang, K. A. Prather, J. Sznitman, J. L. Jimenez, S. S. Lakdawala, Z. Tufekci, L. C. Marr, Airborne transmission of respiratory viruses, *Science* 373 (2021) eabd9149. URL: <https://www.science.org/doi/abs/10.1126/science.abd9149>. doi:10.1126/science.abd9149. arXiv:<https://www.science.org/doi/pdf/10.1126/science.abd9149>.
- [7] W. F. Wells, et al., On air-borne infection. study ii. droplets and droplet nuclei., *American Journal of Hygiene* 20 (1934) 611–18.
- [8] T. Dauxois, T. Peacock, P. Bauer, C. P. Caulfield, C. Cenedese, C. Górlé, G. Haller, G. N. Ivey, P. F. Linden, E. Meiburg, N. Pinardi, N. M. Vriend, A. W. Woods, Confronting grand challenges in environmental fluid mechanics, *Phys. Rev. Fluids* 6 (2021) 020501. URL: <https://link.aps.org/doi/10.1103/PhysRevFluids.6.020501>. doi:10.1103/PhysRevFluids.6.020501.
- [9] G. Tryggvason, R. Scardovelli, S. Zaleski, *Direct numerical simulations of gas-liquid multiphase flows*, Cambridge university press, 2011.
- [10] G. Son, V. K. Dhir, Numerical Simulation of Film Boiling Near Critical Pressures With a Level Set Method, *Journal of Heat Transfer* 120 (1998) 183–192. doi:10.1115/1.2830042.
- [11] F. Gibou, R. Fedkiw, A fourth order accurate discretization for the laplace and heat equations on arbitrary domains, with applications to the stefan problem, *Journal of Computational Physics* 202 (2005) 577–601. URL: <https://www.sciencedirect.com/science/article/pii/S0021999104002980>. doi:<https://doi.org/10.1016/j.jcp.2004.07.018>.
- [12] S. Tanguy, M. Sagan, B. Lalanne, F. Couderc, C. Colin, Benchmarks and numerical methods for the simulation of boiling flows, *Journal of Computational Physics* 264 (2014) 1–22. URL: <https://www.sciencedirect.com/630science/article/pii/S0021999114000412>. doi:<https://doi.org/10.1016/j.jcp.2014.01.014>.
- [13] L. R. Villegas, R. Alis, M. Lepilliez, S. Tanguy, A ghost fluid/level set method for boiling flows and liquid evaporation: Application to the leidenfrost effect, *Journal of Computational Physics* 316

- (2016) 789–813. URL: <https://www.sciencedirect.com/science/article/pii/S0021999116300778>. doi:<https://doi.org/10.1016/j.jcp.2016.04.031>.
- [14] M. S. Lee, A. Riaz, V. Aute, Direct numerical simulation of incompressible multiphase flow with phase change, *Journal of Computational Physics* 344 (2017) 381–418. URL: <https://www.sciencedirect.com/science/article/pii/S0021999117303613>. doi:<https://doi.org/10.1016/j.jcp.2017.04.073>.
- [15] Z. Ge, J.-C. Loiseau, O. Tammisola, L. Brandt, An efficient mass-preserving interface-correction level set/ghost fluid method for droplet suspensions under depletion forces, *Journal of Computational Physics* 353 (2018) 435–459. URL: <https://www.sciencedirect.com/science/article/pii/S0021999117308136>. doi:<https://doi.org/10.1016/j.jcp.2017.10.046>.
- [16] K. Luo, C. Shao, M. Chai, J. Fan, Level set method for atomization and evaporation simulations, *Progress in Energy and Combustion Science* 73 (2019) 65–94. URL: <https://www.sciencedirect.com/science/article/pii/S0360128518301710>. doi:<https://doi.org/10.1016/j.pecs.2019.03.001>.
- [17] J. Schlottke, B. Weigand, Direct numerical simulation of evaporating droplets, *Journal of Computational Physics* 227 (2008) 5215–5237. URL: <https://www.sciencedirect.com/science/article/pii/S0021999108000740>. doi:<https://doi.org/10.1016/j.jcp.2008.01.042>.
- [18] J. Ma, D. Bothe, Numerical modeling of thermocapillary two-phase flows with evaporation using a two-scalar approach for heat transfer, *Journal of Computational Physics* 233 (2013) 552–573. URL: <https://www.sciencedirect.com/science/article/pii/S0021999112005426>. doi:<https://doi.org/10.1016/j.jcp.2012.09.011>.
- [19] J. Palmore, O. Desjardins, A volume of fluid framework for interface-resolved simulations of vaporizing liquid-gas flows, *Journal of Computational Physics* 399 (2019) 108954. URL: <https://www.sciencedirect.com/science/article/pii/S0021999119300778>.

sciencedirect.com/science/article/pii/S002199911930659X.
doi:<https://doi.org/10.1016/j.jcp.2019.108954>.

- [20] J. Reutzsch, C. Kieffer-Roth, B. Weigand, A consistent method for direct numerical simulation of droplet evaporation, *Journal of Computational Physics* 413 (2020) 109455. URL: <https://www.sciencedirect.com/science/article/pii/S0021999120302291>. doi:<https://doi.org/10.1016/j.jcp.2020.109455>.
- [21] N. Scapin, P. Costa, L. Brandt, A volume-of-fluid method for interface-resolved simulations of phase-changing two-fluid flows, *Journal of Computational Physics* 407 (2020) 109251. URL: <https://www.sciencedirect.com/science/article/pii/S0021999120300255>. doi:<https://doi.org/10.1016/j.jcp.2020.109251>.
- [22] L. Malan, A. Malan, S. Zaleski, P. Rousseau, A geometric vof method for interface resolved phase change and conservative thermal energy advection, *Journal of Computational Physics* 426 (2021) 109920. URL: <https://www.sciencedirect.com/science/article/pii/S002199912030694X>. doi:<https://doi.org/10.1016/j.jcp.2020.109920>.
- [23] V. Boniou, T. Schmitt, A. Vié, Consistency and accuracy in the simulation of two phase flows with phase change using sharp interface capturing methods, *Journal of Computational Physics* 470 (2022) 111604. URL: <https://www.sciencedirect.com/science/article/pii/S0021999122006660>. doi:<https://doi.org/10.1016/j.jcp.2022.111604>.
- [24] B. Boyd, Y. Ling, A consistent volume-of-fluid approach for direct numerical simulation of the aerodynamic breakup of a vaporizing drop, *Computers & Fluids* 254 (2023) 105807. URL: <https://www.sciencedirect.com/science/article/pii/S0045793023000324?via%3Dihub>. doi:<https://doi.org/10.1016/j.compfluid.2023.105807>.
- [25] S. W. Welch, J. Wilson, A volume of fluid based method for fluid flows with phase change, *Journal of Computational Physics* 160 (2000) 662–682. URL: <https://www.sciencedirect.com/science/article/>

pii/S0021999100964817. doi:<https://doi.org/10.1006/jcph.2000.6481>.

- [26] G. Tryggvason, B. Bunner, A. Esmaeeli, D. Juric, N. Al-Rawahi, W. Tauber, J. Han, S. Nas, Y.-J. Jan, A front-tracking method for the computations of multiphase flow, *Journal of computational physics* 169 (2001) 708–759.
- [27] D. Juric, G. Tryggvason, Computations of boiling flows, *International journal of multiphase flow* 24 (1998) 387–410.
- [28] M. Muradoglu, G. Tryggvason, A front-tracking method for computation of interfacial flows with soluble surfactants, *Journal of computational physics* 227 (2008) 2238–2262.
- [29] M. Muradoglu, G. Tryggvason, Simulations of soluble surfactants in 3d multiphase flow, *Journal of Computational Physics* 274 (2014) 737–757.
- [30] N. Al-Rawahi, G. Tryggvason, Numerical simulation of dendritic solidification with convection: Two-dimensional geometry, *Journal of Computational Physics* 180 (2002) 471–496. URL: <https://www.sciencedirect.com/science/article/pii/S0021999102970920>. doi:<https://doi.org/10.1006/jcph.2002.7092>.
- [31] D. Izbassarov, M. Muradoglu, A front-tracking method for computational modeling of viscoelastic two-phase flow systems, *Journal of Non-Newtonian Fluid Mechanics* 223 (2015) 122–140. URL: <https://www.sciencedirect.com/science/article/pii/S0377025715001214>. doi:<https://doi.org/10.1016/j.jnnfm.2015.05.012>.
- [32] A. Esmaeeli, G. Tryggvason, Computations of explosive boiling in microgravity, *Journal of scientific computing* 19 (2003) 163–182.
- [33] A. Esmaeeli, G. Tryggvason, Computations of film boiling. part i: numerical method, *International Journal of Heat and Mass Transfer* 47 (2004) 5451–5461. URL: <https://www.sciencedirect.com/science/article/pii/S0017931004002947>. doi:<https://doi.org/10.1016/j.ijheatmasstransfer.2004.07.027>.

- [34] A. Esmaeeli, G. Tryggvason, Computations of film boiling. part ii: multi-mode film boiling, *International Journal of Heat and Mass Transfer* 47 (2004) 5463–5476. URL: <https://www.sciencedirect.com/science/article/pii/S0017931004002959>. doi:<https://doi.org/10.1016/j.ijheatmasstransfer.2004.07.028>.
- [35] A. Koynov, J. G. Khinast, G. Tryggvason, Mass transfer and chemical reactions in bubble swarms with dynamic interfaces, *AIChE journal* 51 (2005) 2786–2800.
- [36] B. Aboulhasanzadeh, S. Thomas, M. Taeibi-Rahni, G. Tryggvason, Multiscale computations of mass transfer from buoyant bubbles, *Chemical Engineering Science* 75 (2012) 456–467. URL: <https://www.sciencedirect.com/science/article/pii/S000925091200231X>. doi:<https://doi.org/10.1016/j.ces.2012.04.005>.
- [37] M. Irfan, M. Muradoglu, A front tracking method for direct numerical simulation of evaporation process in a multiphase system, *Journal of Computational Physics* 337 (2017) 132–153.
- [38] M. Irfan, M. Muradoglu, A front tracking method for particle-resolved simulation of evaporation and combustion of a fuel droplet, *Computers & Fluids* 174 (2018) 283–299.
- [39] A. Khorram, S. Mortazavi, Direct numerical simulation of film boiling on a horizontal periodic surface in three dimensions using front tracking, *Physics of Fluids* 34 (2022).
- [40] M. Najafian, S. Mortazavi, A numerical study of drop evaporation at high density ratios using front-tracking method, *Computers & Mathematics with Applications* 134 (2023) 1–15. URL: <https://www.sciencedirect.com/science/article/pii/S0898122122005247>. doi:<https://doi.org/10.1016/j.camwa.2022.12.019>.
- [41] R. Mittal, H. Dong, M. Bozkurttas, F. Najjar, A. Vargas, A. Von Loebbecke, A versatile sharp interface immersed boundary method for incompressible flows with complex boundaries, *Journal of computational physics* 227 (2008) 4825–4852.

- [42] Y. Sato, B. Ničeno, A sharp-interface phase change model for a mass-conservative interface tracking method, *Journal of Computational Physics* 249 (2013) 127–161.
- [43] P. Bhuvankar, S. Dabiri, Numerical simulation of sliding bubbles in saturated flow boiling, *Chemical Engineering Science* 228 (2020) 115919. URL: <https://www.sciencedirect.com/science/article/pii/S0009250920304516>. doi:<https://doi.org/10.1016/j.ces.2020.115919>.
- [44] A. Esmaeeli, G. Tryggvason, A front tracking method for computations of boiling in complex geometries, *International Journal of Multiphase Flow* 30 (2004) 1037–1050.
- [45] S. O. Unverdi, G. Tryggvason, A front-tracking method for viscous, incompressible, multi-fluid flows, *Journal of computational physics* 100 (1992) 25–37.
- [46] A. Esmaeeli, G. Tryggvason, Computations of film boiling. part ii: multi-mode film boiling, *International journal of heat and mass transfer* 47 (2004) 5463–5476.
- [47] A. J. Chorin, Numerical solution of the navier-stokes equations, *Mathematics of computation* 22 (1968) 745–762.
- [48] J. C. Adams, Mudpack: Multigrid portable fortran software for the efficient solution of linear elliptic partial differential equations., *Appl Math Comput* 34 (1989) 113–146. URL: <https://www.sciencedirect.com/science/article/abs/pii/0096300389900106>. doi:[https://doi.org/10.1016/0096-3003\(89\)90010-6](https://doi.org/10.1016/0096-3003(89)90010-6).
- [49] B. Leonard, A stable and accurate convective modelling procedure based on quadratic upstream interpolation, *Computer Methods in Applied Mechanics and Engineering* 19 (1979) 59–98. URL: <https://www.sciencedirect.com/science/article/pii/0045782579900343>. doi:[https://doi.org/10.1016/0045-7825\(79\)90034-3](https://doi.org/10.1016/0045-7825(79)90034-3).
- [50] R. Borges, M. Carmona, B. Costa, W. S. Don, An improved weighted essentially non-oscillatory scheme for hyperbolic conservation laws, *Journal of computational physics* 227 (2008) 3191–3211.

- [51] H. Zolfaghari, D. Izbassarov, M. Muradoglug, Simulations of viscoelastic two-phase flows in complex geometries, *Computers and Fluids* 156 (2017) 548–561.
- [52] C. S. Peskin, Numerical analysis of blood flow in the heart, *Journal of computational physics* 25 (1977) 220–252.
- [53] J. Han, G. Tryggvason, Secondary breakup of axisymmetric liquid drops. i. acceleration by a constant body force, *Physics of fluids* 11 (1999) 3650–3667.
- [54] T. Kalra, P. Uhlherr, Mass transfer between the attached wake of a bluff body and the free stream, *Chemical Engineering Science* 28 (1973) 915–923.
- [55] R. Clift, J. R. Grace, M. E. Weber, *Bubbles, drops, and particles*, Courier Corporation, 2005.
- [56] A. G. TOMBOULIDES, S. A. ORSZAG, Numerical investigation of transitional and weak turbulent flow past a sphere, *Journal of Fluid Mechanics* 416 (2000) 45–73. doi:10.1017/S0022112000008880.
- [57] P. Bagchi, M. Ha, S. Balachandar, Direct numerical simulation of flow and heat transfer from a sphere in a uniform cross-flow, *J. Fluids Eng.* 123 (2001) 347–358.
- [58] I. M. Rodríguez Pérez, O. Lehmkuhl, M. Soria Guerrero, S. Gómez, M. Domínguez Pumar, L. Kowalski, et al., On the boundary layer development and heat transfer from a sphere at moderate reynolds numbers, in: *Tenth International Conference on Computational Fluid Dynamics (ICCFD10)*, 2018, pp. 1–14. doi:http://hdl.handle.net/2117/119563.
- [59] S. Majumdar, G. Iaccarino, P. Durbin, et al., Rans solvers with adaptive structured boundary non-conforming grids, *Annual Research Briefs* 1 (2001) 179.
- [60] S. Turns, *An Introduction to Combustion: Concepts and Applications*, McGraw-Hill series in mechanical engineering, McGraw-Hill, 2000. URL: <https://books.google.com.tr/books?id=rzo8PgAACAAJ>.

- [61] F. A. Williams, *Combustion theory*, CRC Press, 2018.
- [62] M. Muradoglu, K. Liu, S. Pope, Pdf modeling of a bluff-body stabilized turbulent flame, *Combustion and Flame* 132 (2003) 115–137.
- [63] M. Muradoglu, G. Tryggvason, Simulations of soluble surfactants in 3d multiphase flow, *Journal of Computational Physics* 274 (2014) 737–757. URL: <https://www.sciencedirect.com/science/article/pii/S0021999114004318>. doi:<https://doi.org/10.1016/j.jcp.2014.06.024>.
- [64] G. Faeth, Current status of droplet and liquid combustion, *Progress in Energy and Combustion Science* 3 (1977) 191–224. URL: <https://www.sciencedirect.com/science/article/pii/0360128577900120>. doi:[https://doi.org/10.1016/0360-1285\(77\)90012-0](https://doi.org/10.1016/0360-1285(77)90012-0).
- [65] W. A. Sirignano, Fuel droplet vaporization and spray combustion theory, *Progress in Energy and Combustion Science* 9 (1983) 291–322. URL: <https://www.sciencedirect.com/science/article/pii/0360128583900114>. doi:[https://doi.org/10.1016/0360-1285\(83\)90011-4](https://doi.org/10.1016/0360-1285(83)90011-4).
- [66] C. Law, Recent advances in droplet vaporization and combustion, *Progress in Energy and Combustion Science* 8 (1982) 171–201. URL: <https://www.sciencedirect.com/science/article/pii/0360128582900119>. doi:[https://doi.org/10.1016/0360-1285\(82\)90011-9](https://doi.org/10.1016/0360-1285(82)90011-9).
- [67] S. S. Sazhin, Modelling of fuel droplet heating and evaporation: Recent results and unsolved problems, *Fuel* 196 (2017) 69–101. URL: <https://www.sciencedirect.com/science/article/pii/S0016236117300583>. doi:<https://doi.org/10.1016/j.fuel.2017.01.048>.
- [68] R. Haywood, M. Renksizbulut, G. Raithby, Transient deformation and evaporation of droplets at intermediate reynolds numbers, *International Journal of Heat and Mass Transfer* 37 (1994) 1401–1409. URL: <https://www.sciencedirect.com/science/article/pii/0017931094901864>. doi:[https://doi.org/10.1016/0017-9310\(94\)90186-4](https://doi.org/10.1016/0017-9310(94)90186-4).

- [69] H. Rusche, Computational fluid dynamics of dispersed two-phase flows at high phase fractions, Ph.D. thesis, Imperial College London (University of London), 2003.
- [70] C. Chauveau, M. Birouk, I. Gökalp, An analysis of the d2-law departure during droplet evaporation in microgravity, *International journal of multiphase flow* 37 (2011) 252–259.
- [71] I. Gokalp, C. Chauveau, J.-R. Richard, M. Kramer, W. Leuckel, Observations on the low temperature vaporization and envelope or wake flame burning of n-heptane droplets at reduced gravity during parabolic flights, in: *Symposium (International) on Combustion*, volume 22, Elsevier, 1989, pp. 2027–2035.
- [72] I. Gökalp, C. Chauveau, O. Simon, X. Chesneau, Mass transfer from liquid fuel droplets in turbulent flow, *Combustion and flame* 89 (1992) 286–298.
- [73] I. Gokalp, C. Chauveau, H. Berrekam, R. NA, Vaporization of miscible binary fuel droplets under laminar and turbulent convective conditions, *Atomization and Sprays* 4 (1994) 661–676.
- [74] U. Olgac, D. Izbassarov, M. Muradoglu, Direct numerical simulation of an oscillating droplet in partial contact with a substrate, *Computers & Fluids* 77 (2013) 152–158.
- [75] S. Tasoglu, G. Kaynak, A. J. Szeri, U. Demirci, M. Muradoglu, Impact of a compound droplet on a flat surface: A model for single cell epitaxy, *Physics of Fluids* 22 (2010) 082103.
- [76] M. Setiya, J. Palmore, Quasi-steady evaporation of deformable liquid fuel droplets, *International Journal of Multiphase Flow* 164 (2023) 104455. URL: <https://www.sciencedirect.com/science/article/pii/S0301932223000769>. doi:<https://doi.org/10.1016/j.ijmultiphaseflow.2023.104455>.
- [77] B. Abramzon, W. A. Sirignano, Droplet vaporization model for spray combustion calculations, *International journal of heat and mass transfer* 32 (1989) 1605–1618.

- [78] W. A. Sirignano, Fluid dynamics and transport of droplets and sprays, Cambridge university press, 2010.
- [79] N. Frössling, The evaporation of falling drops, Gerlands Beitr. Geophys 52 (1938) 170–216.